

# An implementation of radiative transfer in the cosmological simulation code GADGET

Margarita Petkova<sup>1\*</sup> and Volker Springel<sup>1†</sup>

<sup>1</sup>*Max-Planck-Institut für Astrophysik, Karl-Schwarzschild-Strasse 1, 85748 Garching, Germany*

Accepted 2009 March 30. Received 2009 March 27; in original form 2008 December 9

## ABSTRACT

We present a novel numerical implementation of radiative transfer in the cosmological smoothed particle hydrodynamics (SPH) simulation code GADGET. It is based on a fast, robust and photon-conserving integration scheme where the radiation transport problem is approximated in terms of moments of the transfer equation and by using a variable Eddington tensor as a closure relation, following the ‘OTVET’-suggestion of Gnedin & Abel. We derive a suitable anisotropic diffusion operator for use in the SPH discretization of the local photon transport, and we combine this with an implicit solver that guarantees robustness and photon conservation. This entails a matrix inversion problem of a huge, sparsely populated matrix that is distributed in memory in our parallel code. We solve this task iteratively with a conjugate gradient scheme. Finally, to model photon sink processes we consider ionisation and recombination processes of hydrogen, which is represented with a chemical network that is evolved with an implicit time integration scheme. We present several tests of our implementation, including single and multiple sources in static uniform density fields with and without temperature evolution, shadowing by a dense clump, and multiple sources in a static cosmological density field. All tests agree quite well with analytical computations or with predictions from other radiative transfer codes, except for shadowing. However, unlike most other radiative transfer codes presently in use for studying reionisation, our new method can be used on-the-fly during dynamical cosmological simulation, allowing simultaneous treatments of galaxy formation and the reionisation process of the Universe.

**Key words:** radiative transfer - methods: numerical

## 1 INTRODUCTION

The absence of Gunn-Peterson troughs in the spectra of high redshift quasars up to  $z \leq 6$  (Fan et al. 2006; White et al. 2003) suggests that hydrogen is highly ionised at low redshift, with a volume averaged neutral hydrogen fraction of  $x_{\text{HI}} \leq 10^{-4}$  (Fan 2007). The current generation of simulation codes for cosmological structure formation calculates the self-gravity of dark matter and cosmic gas, and the fluid dynamics of the cosmic gas, but radiation processes are typically not taken into account, or only at the level of a spatially uniform, externally imposed background field. However, we know that the radiation field has been highly inhomogeneous during certain phases of the growth of structure, and may have in fact provided important feedback effects for galaxy formation (e.g. Iliev et al. 2005; Yoshida et al. 2007; Croft & Altay 2008). Therefore, it would be ideal to be able

to calculate self-consistent simulations that *simultaneously* follow cosmic structure growth and the ionisation history of the Universe.

However, the high calculation cost and complexity of radiative transfer has so far prevented such simulations, apart from very few exceptions (e.g. Gnedin & Ostriker 1997; Kohler et al. 2007; Shin et al. 2008; Wise & Abel 2008). Instead, the cosmic reionisation process has been most often treated separately in postprocessing, based on static simulated density fields (e.g. Ciardi et al. 2003; Sokasian et al. 2004; Iliev et al. 2006; Zahn et al. 2007; Croft & Altay 2008; Li et al. 2008). It is the goal of this study to develop a new numerical scheme that makes self-consistent radiation-hydrodynamic simulations possible based on the high-resolution Lagrangian cosmological code GADGET-3 (Springel et al. 2001; Springel 2005).

A large number of different approximate methods have been developed to make problems of radiative transfer numerically tractable, which are in their full generality only solvable analytically for very few special cases. The known

\* E-mail: mpetkova@mpa-garching.mpg.de

† E-mail: volker@mpa-garching.mpg.de

numerical methods include long characteristics ray-tracing schemes (Mihalas & Weibel Mihalas 1984; Abel et al. 1999; Sokasian et al. 2001; Cen 2002; Abel & Wandelt 2002; Razoumov & Cardall 2005), short characteristic ray-tracing schemes (Kunasz & Auer 1988; Nakamoto et al. 2001; Mellema et al. 2006; Whalen & Norman 2006; Alvarez et al. 2006; Susa 2006; Altay et al. 2008; Ciardi et al. 2001; Maselli et al. 2003), hybrid ray-tracing schemes (Rijkhorst et al. 2006; Trac & Cen 2007), moment methods and direct solvers (Mellema et al. 1998; Gnedin & Abel 2001; Shapiro et al. 2004; Whitehouse et al. 2005; Aubert & Teyssier 2008; Finlator et al. 2008) and other particle-based transport methods (Ritzerveld et al. 2003; Pawlik & Schaye 2008).

In the long characteristics method each test cell in the computational volume is connected to all other relevant cells. Then the equation of radiative transfer is integrated individually from that test cell to each of the selected cells. While this method is relatively simple and straight-forward, it is also very time consuming, since it requires  $N^2$  interactions between the cells. Moreover, parallelization of this approach is cumbersome and requires large amounts of data exchange between the different processors. Short characteristic methods integrate the equation of radiative transfer along lines that connect nearby cells. Here a cell is connected only to its neighboring cells, and not to all other cells in the computational domain. This reduces the redundancy of the computations and makes the scheme easier to parallelize.

Stochastic integration methods, specifically Monte Carlo methods, employ a ray-tracing strategy where the rays are discretized into photon packets. For each photon packet, the emission, its frequency and its direction of propagation are determined by sampling the appropriate distribution functions that have been assigned in the initial conditions. A particular advantage of this approach is that comparatively few approximations to the radiative transfer equations need to be made, so that the quality of the results is primarily a function of the number of photon packets employed, which can be made larger in proportion to the CPU time spent. A disadvantage of these scheme is the comparatively high computational cost and the sizable level of noise in the discretized radiation field.

Using moments of the radiative transfer equations instead of the full radiative transfer equation can lead to very substantial simplifications that can drastically speed up the calculations. In this approach, the radiation is represented by its mean intensity field throughout the computational domain. Instead of following rays, the moment equations are solved directly on the grid or for the particles. Due to its local nature, the moment approach is comparatively easy to parallelize, but it of course depends on the nature of the investigated problem whether the simplifications made still provide sufficient accuracy.

In this paper we develop a moments method that is closely related in spirit to the Optically Thin Variable Eddington Tensor (OTVET) scheme proposed by Gnedin & Abel (2001). However, we try to implement it directly on top of the irregular set of positions sampled by the particles of Smoothed Particle Hydrodynamics (SPH) simulations, and we use quite different numerical techniques to solve the resulting transport equations. In OTVET, the system of moment equations is closed by estimating the local

Eddington tensor with a simple optical thin approximation, i.e. one pretends that all sources of light are ‘visible’ at a given location. Once the Eddington tensors are found, the local radiation transfer reduces to an anisotropic diffusion problem. The particular attraction of this moment-based formulation is that it is potentially very fast, allowing a direct coupling with cosmological hydrodynamic simulations. In particular, if a rapid method for calculating the Eddington tensors can be found, the scheme should be able to easily deal with an arbitrary number of sources. Also, the radiation intensity field does not suffer from the Poisson shot noise inherent in Monte Carlo approaches. Together with the local nature of the diffusion problem, this makes this approach particularly attractive for trying to address the cosmological reionisation problem with self-consistent simulations of galaxy formation, since it is likely that low-mass star-forming galaxies of high number density play an important role for the reionisation process. We therefore adopt in this paper the suggestion of Gnedin & Abel (2001) and work out an implementation of the OTVET scheme in SPH. As we shall see, this entails a number of numerical challenges in practice. We will describe our solutions for these problems, and carry out a number of tests to evaluate the accuracy of the resulting implementation.

The near complete lack of analytical results for non-trivial radiative transfer problems makes it actually hard to validate different numerical techniques and to compare their performance with each other. A very useful help in this respect is provided by the cosmological radiative transfer code comparison project, carried out by Iliev et al. (2006). In their paper, they present a comparison of 11 independent cosmological radiative transfer codes when applied to a variety of different test problems. A number of our tests are based on this study, which hence allows a comparison with results of these other codes.

We start this paper with a brief introduction to the radiative transfer equations in Section 2. We then describe in Section 3 the moment-based method that is the basis for our approximate treatment of the radiation transfer problem. In Section 4 we elaborate in detail the numerical implementation of this scheme in SPH. This is followed by a presentation of results for various test problems in Section 5. Finally, we conclude with a summary and an outlook in Section 6. In an appendix, we give for reference further details on our rate equations, and on the conjugate gradient approach.

## 2 THE RADIATIVE TRANSFER PROBLEM

### 2.1 Equation of radiative transfer

Let us briefly derive the radiative transfer (RT) equation in comoving coordinates, which is also useful for introducing our notation. Let  $f_\gamma(t, \mathbf{x}, \mathbf{p})$  be the photon distribution function for comoving coordinates  $\mathbf{x}$  and comoving photon momentum

$$\mathbf{p} = a \frac{h\nu}{c} \hat{\mathbf{n}}, \quad (1)$$

where  $a \equiv a(t)$  is the cosmological scale factor,  $h$  is the Planck constant,  $\nu$  is the frequency of the photons, and  $\hat{\mathbf{n}}$  is the unit vector in the direction of photon propagation. Then the number of photons in some part of the Universe is

$$N_\gamma = \int d\mathbf{x} d\mathbf{p} f_\gamma(t, \mathbf{x}, \mathbf{p}). \quad (2)$$

We can further define the phase-space continuity equation for the distribution function  $f_\gamma \equiv f_\gamma(t, \mathbf{x}, \mathbf{p})$  of photons as

$$\frac{\partial f_\gamma}{\partial t} + \frac{\partial}{\partial \mathbf{x}}(\dot{\mathbf{x}} f_\gamma) + \frac{\partial}{\partial \mathbf{p}}(\dot{\mathbf{p}} f_\gamma) = \left. \frac{\partial f_\gamma}{\partial t} \right|_{\text{sources}} - \left. \frac{\partial f_\gamma}{\partial t} \right|_{\text{sinks}}. \quad (3)$$

Here the source and sink terms on the right hand side of the equation represent photon emission and absorption processes, respectively. We define the specific radiation intensity  $I_\nu$  as the energy of photons in a frequency bin  $\Delta\nu$  that pass through an area  $\Delta A$  and solid angle  $\Delta\Omega$  for a time  $\Delta t$ . The specific intensity  $I_\nu$  is then related to the photon distribution  $f_\gamma$  as follows

$$I_\nu = h\nu f_\gamma \frac{d^3x d^3p}{d\nu d\Omega dA dt} = \frac{h^4 \nu^3}{c^2} f_\gamma. \quad (4)$$

Substituting into equation (3), rearranging and adding the proper absorption and emission terms, one obtains the following radiative transfer equation in comoving variables (Gnedin & Ostriker 1997):

$$\frac{1}{c} \frac{\partial I_\nu}{\partial t} + \frac{\mathbf{n}}{a} \frac{\partial I_\nu}{\partial \mathbf{x}} - \frac{H}{c} \left( \nu \frac{\partial I_\nu}{\partial \nu} - 3I_\nu \right) = -\kappa_\nu I_\nu + j_\nu, \quad (5)$$

where  $H \equiv \dot{a}/a$  is the Hubble expansion rate,  $\kappa_\nu$  is the absorption coefficient and  $j_\nu$  is the emission coefficient.

Unfortunately, this full radiative transfer (RT) equation is in practice very difficult to solve in full generality. In particular, the high dimensionality (comprised of 3 spatial variables, 2 directional angles, 1 frequency variable, and time) of this partial differential equation makes a direct discretization on a mesh highly problematic. We will hence apply in Section 3 simplifications to the RT equation that yield an approximation that can be more easily calculated in cosmological codes.

## 2.2 Basic physics of hydrogen photoionisation

If we consider pure hydrogen gas, the rate equations describing photoionisation and photoheating processes become comparatively simple. For the most part we will restrict ourselves to this chemical composition in this paper, but we note that an extension of our formalism to include other elements is readily possible. In fact, we have already implemented helium as well, but we omit an explicit discussion of it in the following for the sake of simplicity.

The photoionisation rate  $k_{\text{ion}}$  of hydrogen ( $H + h\nu \rightarrow H^+ + e^-$ ) is given by

$$k_{\text{ion}} = \int d\Omega \int_{\nu_o}^{\infty} d\nu \frac{I_\nu \sigma_\nu}{h\nu}, \quad (6)$$

where  $h\nu_o = 13.6 \text{ eV}$  is the hydrogen ionisation potential and  $\sigma_\nu$  is the photoionisation cross-section:

$$\sigma_\nu = \sigma_o \left( \frac{\nu}{\nu_o} \right)^4 \frac{\exp\{4 - [(4 \tan^{-1} \epsilon)/\epsilon]\}}{1 - \exp(-2\pi/\epsilon)} \text{ for } \nu \geq \nu_o, \quad (7)$$

where  $\sigma_o = 6.30 \times 10^{-18} \text{ cm}^2$  and  $\epsilon = \sqrt{(\nu/\nu_o) - 1}$ .

The corresponding photoheating rate of hydrogen is given by

$$\Gamma = n_{\text{HI}} \int d\Omega \int_{\nu_o}^{\infty} d\nu \frac{I_\nu \sigma_\nu}{h\nu} (h\nu - h\nu_o), \quad (8)$$

where  $n_{\text{HI}}$  is the number density of neutral hydrogen. Furthermore, the change in the neutral gas density due to recombinations is given by

$$\frac{\partial n_{\text{HI}}}{\partial t} = \alpha n_e n_p, \quad (9)$$

where  $\alpha$  is the temperature-dependent recombination coefficient,  $n_e$  is the electron number density and  $n_p \equiv n_{\text{HII}}$  is the proton number density, which is in turn equal to the ionised hydrogen number density (for a pure hydrogen gas).

The change of the density of the neutral gas due to ionisations is given by

$$\frac{\partial n_{\text{HI}}}{\partial t} = -c \sigma_o n_{\text{HI}} n_\gamma, \quad (10)$$

where  $c$  is the speed of light and  $n_\gamma$  is the number density of ionising photons. Thus, the total change in the neutral gas density, due to ionisations or recombinations, is given by

$$\frac{\partial n_{\text{HI}}}{\partial t} = \alpha n_e n_{\text{HII}} - c \sigma_o n_{\text{HI}} n_\gamma. \quad (11)$$

For all our calculations described in this paper we use the on-the-spot approximation (Osterbrock & Ferland 2006), i.e. photons emitted due to recombinations to excited levels are re-absorbed immediately by neutral hydrogen atoms in the vicinity. This behavior is described by the so called case-B recombination coefficient  $\alpha_B$ .

## 3 THE VARIABLE EDDINGTON TENSOR FORMALISM

We now turn to a description of the moment-based approximation to the radiation transfer problem that we use in this study. The first three moments of the specific intensity, the mean intensity  $J_\nu$ , the radiation flux vector  $F_\nu^i$ , and the radiation pressure tensor  $P_\nu^{ij}$ , are defined as follows:

$$J_\nu = \frac{1}{4\pi} \int d\Omega I_\nu, \quad (12)$$

$$F_\nu^i = \frac{1}{4\pi} \int d\Omega n^i I_\nu, \quad (13)$$

$$P_\nu^{ij} = \frac{1}{4\pi} \int d\Omega n^i n^j I_\nu, \quad (14)$$

where  $n$  is a direction vector and the indices  $i$  and  $j$  run through the three elements of the vector in Cartesian space. We can further define  $h^{ij}$ , the so-called Eddington tensor, based on  $P_\nu^{ij} = J_\nu h^{ij}$ .

We can for the moment ignore the frequency derivative in the RT equation if we can assume that the Universe does not expand significantly before a photon is absorbed. With this simplification, the first moments of the RT equation take the form:

$$\frac{1}{c} \frac{\partial J_\nu}{\partial t} + \frac{1}{a} \frac{\partial F_\nu^i}{\partial x^i} = -\hat{\kappa}_\nu J_\nu + j_\nu, \quad (15)$$

$$\frac{1}{c} \frac{\partial F_\nu^j}{\partial t} + \frac{1}{a} \frac{\partial J_\nu h^{ij}}{\partial x^i} = -\hat{\kappa}_\nu F_\nu^j, \quad (16)$$

where

$$\hat{\kappa}_\nu = \kappa_\nu + \frac{3H}{c}. \quad (17)$$

In the second moment equation (16), we can ignore the term of the order  $c^{-1}$  and solve for the flux

$$F_\nu^j = -\frac{1}{\hat{\kappa}_\nu} \frac{1}{a} \frac{\partial J_\nu h^{ij}}{\partial x^i}, \quad (18)$$

which we then insert back into equation (15). This leads to the following approximation to the RT equation:

$$\frac{\partial J_\nu}{\partial t} = \frac{c}{a^2} \frac{\partial}{\partial x_j} \left( \frac{1}{\hat{\kappa}_\nu} \frac{\partial J_\nu h^{ij}}{\partial x_i} \right) - c \hat{\kappa}_\nu J_\nu + c j_\nu. \quad (19)$$

This form of the RT equation is already much simpler than the fully general form of equation (5). In particular, each of the terms in equation (19) has a simple physical interpretation. The time evolution of the local mean radiation intensity is given by a transport term, described by the anisotropic diffusion term on the right hand side, a sink term describing absorptions, and an emission term that accounts for sources. However, in order to be able to solve this equation an expression for the Eddington tensor  $h^{ij}$  is needed, which is left undefined by these moment equations. We therefore need to assume a certain form for the Eddington tensor, or in other words, a *closure relation*.

For the closure relation, we follow Gnedin & Abel (2001) and estimate the local Eddington tensor with an optically thin approximation. This means that we assume that a reasonable approximation to the Eddington tensor can be obtained by approximating all lines-of-sight to the sources as being optically thin. The radiation intensity pressure tensor  $P^{ij}$  in this optically thin regime can then be computed as

$$P^{ij} \propto \int d^3 x' \rho_*(\mathbf{x}') \frac{(\mathbf{x} - \mathbf{x}')_i (\mathbf{x} - \mathbf{x}')_j}{(\mathbf{x} - \mathbf{x}')^4}, \quad (20)$$

and thus the Eddington tensor is given by

$$h^{ij} = \frac{P^{ij}}{\text{Tr}(P)}. \quad (21)$$

Note that the Eddington tensor only determines in which *direction* the local radiation propagates, but the magnitude of the radiation intensity tensor is unimportant as far as the Eddington tensor is concerned. This means that even in situations where the lines-of-sight to the sources are not optically thin at all, one will often end up with fairly accurate estimates of the Eddington tensor based on equations (20) and (21), simply because the radiation will typically mainly propagate away from the sources, even in optically thick cases. In particular, note that the above approximation is always correct for a single source. When there are multiple sources of equal strength, the optically thin approximation will weight the sources that are closest most strongly, in accordance with the  $1/r^2$  decay of the intensity. While this can be expected to result in reasonably accurate estimates of the Eddington tensor in many situations (especially in the vicinity of a dominating source), errors can certainly arise in particular situations, for example at locations that are equidistant from two sources of equal strength. How serious these errors are in problems of interest needs to be analyzed with appropriate test problems.

As we describe later in more detail in Section 4.8, we note that equation (20) can be accurately calculated with a hierarchical multipole approach similar to the one applied in gravitational tree algorithms. This allows a fairly efficient treatment of an arbitrarily large number of sources, which is a distinctive advantage of the moments based approach compared with other methods.

### 3.1 Choice of convenient Lagrangian variables

We will now rewrite the RT equations into a form that is more convenient for use with a Lagrangian method such as SPH. In particular, it is advantageous to pick variables in the numerical scheme that are normalized to unit mass, not unit volume. For example, if we express the ionisation state of the gas as the number density of ionised hydrogen per unit volume, then we have to readjust this number somehow any time we reestimate the local gas density (which may change if the gas moves around), otherwise the ionised fraction would change. However, if we use convenient variables that are normalized to unit mass, we do not need to worry about such corrections.

For chemical networks of hydrogen, it is convenient (and often done in practice) to express abundances relative to the total abundance of hydrogen nuclei:

$$n_{\text{H}} = \frac{X_{\text{H}} \rho}{m_{\text{p}}}. \quad (22)$$

Here  $X_{\text{H}} = 0.76$  is the cosmological mass fraction of hydrogen and  $m_{\text{p}}$  is the proton mass. In the following, we use the notation  $n_{\text{HI}}$  for neutral hydrogen, and  $n_{\text{HII}}$  for ionised hydrogen, such that

$$n_{\text{H}} = n_{\text{HI}} + n_{\text{HII}}. \quad (23)$$

In our actual numerical code, we will use a variable  $\tilde{n}_{\text{HII}}$  to express the abundance of ionised hydrogen, defined as

$$\tilde{n}_{\text{HII}} = \frac{n_{\text{HII}}}{n_{\text{H}}}, \quad (24)$$

where  $n_{\text{HII}}$  is the ordinary number density of HII atoms (i.e. number of protons per unit volume). Note that this quantity is now normalized to unit mass, as desired. In addition, it is dimensionless, which avoids numerical problems due to large numbers if we use astronomical length units.

A similar reasoning also applies to the radiation intensity itself. In principle, the fundamental quantity we work with is the frequency dependent, angle-averaged mean intensity. However, we cannot afford to carry around a full spectrum with each fluid element in a hydrodynamical code. This would be too cumbersome and also is not really necessary if we are interested only in the reionisation problem. Instead, it is sufficient to store the intensity integrated over a narrow frequency interval around the ionisation potential of hydrogen. Or in other words, a more convenient quantity to work with would be something like the number density of photons capable of ionising hydrogen. We now formulate the relevant equations using this concept.

In general, the photon number density is

$$n_\gamma = \frac{1}{c} \int \frac{4\pi J_\nu}{h\nu} d\nu. \quad (25)$$

However, we will only consider the spectrum in a small band around the frequencies of interest. For simplicity, we assume that the spectrum has the form

$$J_\nu = J_0 \delta(\nu - \nu_0) \quad (26)$$

around the ionisation frequency  $\nu_0$ , where  $h\nu_0 = 13.6 \text{ eV}$  is the hydrogen ionisation potential. This form of the radiation intensity limits the spectrum to effectively just the hydrogen ionisation frequency. We therefore obtain this simple form

$$n_\gamma = \frac{1}{c} \frac{4\pi J_0}{h\nu_0} \quad (27)$$

for the number density of ionising photons.

We also note that the absorption coefficient  $\kappa_\nu$  for ionisation in the equation for radiation transport is

$$\kappa_\nu = n_{\text{HI}} \sigma_\nu, \quad (28)$$

where  $\sigma_\nu$  is the cross-section for hydrogen ionisation. If we multiply the loss term  $\kappa_\nu J_\nu$  in the RT equation by  $4\pi/(c h \nu)$  and integrate over  $\nu$ , we get the so-called ionisation rate  $k_{\text{ion}}$ , given by

$$k_{\text{ion}} = \int \frac{4\pi J_\nu}{h\nu} \sigma_\nu d\nu. \quad (29)$$

For our narrow spectrum, this leads to the simple expression

$$\int d\nu \frac{4\pi}{c h \nu} \kappa_\nu J_\nu = \sigma_0 n_{\text{HI}} n_\gamma, \quad (30)$$

where  $\sigma_0$  is the cross section at the resonance. Another consequence of these definitions is that we can write the number density evolution of ionised hydrogen due to new reionisations as

$$\frac{dn_{\text{HII}}}{dt} = c \sigma_0 n_\gamma n_{\text{HI}}. \quad (31)$$

The photon field loses energy at the same rate, i.e. the loss term for the radiation field should be of the form

$$\frac{dn_\gamma}{dt} = -c \sigma_0 n_\gamma n_{\text{HI}}, \quad (32)$$

which is also what the loss term in the RT equation gives in this notation.

The above suggests that we can cast the moment-based RT equation into a more convenient form if we multiply it through with  $4\pi/(c h \nu)$  and integrate over  $\nu$ . This gives:

$$\frac{\partial n_\gamma}{\partial t} = c \frac{\partial}{\partial x_j} \left( \frac{1}{\kappa} \frac{\partial n_\gamma h^{ij}}{\partial x_i} \right) - c \kappa n_\gamma + s_\gamma, \quad (33)$$

where  $\kappa = \sigma_0 n_{\text{HI}}$  and the cosmological scale factor has been dropped for simplicity. The source function  $s_\gamma$  gives the rate per unit volume at which new ionising photons are produced.

Finally, we also want to express the photon number density in terms of the local density of hydrogen atoms,  $\tilde{n}_\gamma = n_\gamma/n_{\text{H}}$ . Then we get:

$$\frac{\partial \tilde{n}_\gamma}{\partial t} = c \frac{\partial}{\partial x_j} \left( \frac{1}{\kappa} \frac{\partial \tilde{n}_\gamma h^{ij}}{\partial x_i} \right) - c \kappa \tilde{n}_\gamma + \tilde{s}_\gamma. \quad (34)$$

This is the formulation of the RT equation that we implemented in this work in the simulation code GADGET-3.

We have to augment equation (34) with the changes of the different chemical species as a result of interactions with the radiation field. If we consider only hydrogen, this is just:

$$\frac{\partial \tilde{n}_{\text{HII}}}{\partial t} = c \sigma_0 n_{\text{H}} \tilde{n}_{\text{HI}} \tilde{n}_\gamma - \alpha n_{\text{H}} \tilde{n}_e \tilde{n}_{\text{HII}}, \quad (35)$$

where  $\alpha$  is the temperature-dependent recombination coefficient. If we have only hydrogen, we can set  $\tilde{n}_e = \tilde{n}_{\text{HII}}$  and  $\tilde{n}_{\text{HI}} = 1 - \tilde{n}_{\text{HII}}$ .

For hydrogen reionisation problems, we want to solve the two basic equations (34) and (35) as efficiently, accurately and robustly as possible. We recall that the three terms of (34) have a straightforward interpretation. The

first term on the right hand side is a diffusion like equation, which is conservative, i.e. it leaves the total number of photons unchanged. The second term describes photon losses, and each photon lost will cause one hydrogen atom to be ionised. Finally, the third term is the source term, and describes the injection of new photons. This suggests that the total number of ionisations must always be equal to the total number of photons lost. If we can maintain numerically accurate photon conservation, then this property should ensure a proper speed of the ionisation front even for relatively inaccurate time stepping, as the propagation of the front should largely be determined by the injection rate of photons at the source.

The above suggests a simple possibility for treating the time evolution of the photon number density in each timestep in terms of three parts, corresponding to an *operator-splitting*, or *fractional-step* approach: One may first inject new photons according to the source function, then transport photons conservatively by treating the diffusion part, and finally, advance the “chemical network” (eqn. 35) by treating only ionisations and recombinations, making sure again that we do not lose any photons. The chemical equations can be easily “subcycled” or treated with an integrator for stiff differential equations, if needed, because they are completely local. On the other hand, the most expensive part of the time advance is given by the diffusion part. This not only involves a coupling with neighboring fluid elements but also cannot easily be integrated with an explicit time integration scheme, because the diffusion equation becomes easily unstable in this case. We will therefore treat this part with an implicit method. While involving an expensive iteration scheme, this provides good stability and allows for comparatively large timesteps.

## 4 NUMERICAL IMPLEMENTATION

In this section we describe the numerical formalism we have implemented in order to solve the moment-based RT equations coupled to the parallel Tree/SPH code GADGET-3, which is a significantly evolved and extended version of the public GADGET-2 code (Springel 2005). We first give a very brief overview of the basic concepts of smoothed particle hydrodynamics (SPH), and then present a derivation of a new anisotropic diffusion operator in SPH, which is needed for the radiation transfer in moment form when a spatially varying Eddington tensor is used. We also explain how the diffusion equation can be integrated robustly in time based on an implicit scheme with an iterative sparse matrix solver. The time integration of the rate equations for ionisation and recombination also requires special methods because they involve stiff differential equations. Finally, we describe the calculation of the Eddington tensors, and how this can be best combined existing algorithms in the GADGET-3 code.

### 4.1 The basics of smoothed particle hydrodynamics

SPH is a widely used Lagrangian scheme that follows the evolution of gas properties based on discrete tracer particles (see, e.g., Monaghan 1992, for a review). The particle properties are averaged, ‘smoothed’, over a kernel function,

yielding so-called kernel interpolants for the fluid properties based on a few sampling points. For example, the kernel-interpolant of a property  $\langle A \rangle$  is given by

$$\langle A(\mathbf{r}) \rangle = \int d\mathbf{r}' A(\mathbf{r}') W(|\mathbf{r}' - \mathbf{r}|, h), \quad (36)$$

where  $h$  is called the smoothing length and is defined such that the kernel  $W$  drops to zero for  $|\mathbf{r}'| > h$ . In a discretized form this equation becomes

$$\langle A(\mathbf{r}_i) \rangle = \sum_j \frac{m_j}{\rho_j} A(\mathbf{r}_j) W(|\mathbf{r}_j - \mathbf{r}_i|, h_i), \quad (37)$$

where the sum is over all the particles that lie inside radius  $h$ . In the GADGET code, the kernel has the following standard spline form:

$$W(r) = \frac{8}{\pi h^3} \begin{cases} 1 - 6 \left(\frac{r}{h}\right)^2 + 6 \left(\frac{r}{h}\right)^3 & \text{for } 0 \leq \frac{r}{h} \leq \frac{1}{2} \\ 2 \left(1 - \frac{r}{h}\right)^3 & \text{for } \frac{1}{2} < \frac{r}{h} \leq 1 \\ 0 & \text{for } 1 < \frac{r}{h} \end{cases} \quad (38)$$

An important property of the kernel interpolant is that it can also be used to obtain a derivative of the reconstructed function, which can be simply approximated by

$$\begin{aligned} \nabla_i A(\mathbf{r}_i) &= \nabla_i \sum_j \frac{m_j}{\rho_j} A(\mathbf{r}_j) W(|\mathbf{r}_j - \mathbf{r}_i|, h_i) \\ &= \sum_j \frac{m_j}{\rho_j} A(\mathbf{r}_j) \nabla_i W(|\mathbf{r}_j - \mathbf{r}_i|, h_i). \end{aligned} \quad (39)$$

Starting from a density estimate in the form

$$\rho_i = \sum_j m_j W(|\mathbf{r}_j - \mathbf{r}_i|, h_i), \quad (40)$$

this allows one to calculate pressure gradients, and from this, equations of motion for the gas elements which represent the Euler equations. The particular formulation for the equation of motion we use here is based on the ‘entropy-formulation’ of SPH discussed by Springel & Hernquist (2002).

## 4.2 Obtaining anisotropic second order derivatives with a kernel interpolant

Discretization of the diffusion term in the RT transfer equation in SPH poses some difficulties. We are basically confronted with the task to find an efficient and accurate approximation to terms of the form

$$\frac{\partial^2 Q_{\alpha\beta}}{\partial x_s \partial x_k}, \quad (41)$$

where  $Q_{\alpha\beta}$  is the product of the local Eddington tensor  $\mathbf{h}$  and the relative photon density  $\tilde{n}_\gamma$ . Simply differentiating a kernel interpolant twice is not a good solution, as this becomes very noisy because the kernel-interpolant of SPH is only second-order accurate. On the other hand, the discretization of the Laplacian discussed by Jubelgas et al. (2004) does not work either, as it only works for the isotropic case.

We now describe the solution we have found for this problem, which basically consists of the task to approximate the second order partial derivatives of an element  $Q_{\alpha\beta}(\mathbf{x})$  of the matrix  $\mathbf{Q}(\mathbf{x})$  with a kernel-interpolant. We consider a Taylor-series for  $Q_{\alpha\beta}(\mathbf{x}_j)$  in the proximity of  $Q_{\alpha\beta}(\mathbf{x}_i)$ , i.e.

$$\begin{aligned} Q_{\alpha\beta}(\mathbf{x}_j) - Q_{\alpha\beta}(\mathbf{x}_i) &= \nabla Q_{\alpha\beta} \Big|_{\mathbf{x}_i} \cdot (\mathbf{x}_j - \mathbf{x}_i) + \\ &\frac{1}{2} \sum_{s,k} \frac{\partial^2 Q_{\alpha\beta}}{\partial x_s \partial x_k} \Big|_{\mathbf{x}_i} (\mathbf{x}_j - \mathbf{x}_i)_s (\mathbf{x}_j - \mathbf{x}_i)_k + \\ &\mathcal{O}(\mathbf{x}_j - \mathbf{x}_i)^3. \end{aligned} \quad (42)$$

Let us use the short-hand notation  $\mathbf{x}_{ij} = \mathbf{x}_j - \mathbf{x}_i$  and  $W_{ij} = W(|\mathbf{x}_j - \mathbf{x}_i|)$ , where  $W(r)$  is the SPH smoothing kernel. Neglecting higher order terms, we multiply the above expansion with

$$\frac{(\mathbf{x}_{ij})_l W_{ij,m}}{|\mathbf{x}_{ij}|^2}, \quad (43)$$

and integrate over all  $\mathbf{x}_j$ . Here  $(\mathbf{x}_{ij})_l$  is the  $l$ -th component of the vector  $\mathbf{x}_{ij}$ , and  $W_{ij,m}$  is the partial derivative of  $W_{ij}$  with respect to the  $m$ -component of  $\mathbf{x}_i$ . In particular, this means we have

$$\begin{aligned} W_{ij,m} &= (\nabla_i W_{ij})_m = -(\nabla_j W_{ij})_m = \frac{\partial W(|\mathbf{x}_{ij}|)}{\partial (\mathbf{x}_i)_m} \\ &= -W'(|\mathbf{x}_{ij}|) \frac{(\mathbf{x}_{ij})_m}{|\mathbf{x}_{ij}|}. \end{aligned} \quad (44)$$

We now find that

$$\int \frac{(\mathbf{x}_{ij})_k (\mathbf{x}_{ij})_l W_{ij,m}}{|\mathbf{x}_{ij}|^2} d\mathbf{x}_j = 0, \quad (45)$$

for all combinations of  $k$ ,  $l$  and  $m$ . This is because there is always at least one single component of  $\mathbf{x}_{ij}$  left so that the integral vanishes by symmetry. As a result, the first order term of our integrated Taylor expansion drops out.

We now consider the second order term, where we encounter the expression

$$T_{sklm} = \int \frac{(\mathbf{x}_{ij})_s (\mathbf{x}_{ij})_k (\mathbf{x}_{ij})_l (\mathbf{x}_{ij})_m W'(|\mathbf{x}_{ij}|)}{|\mathbf{x}_{ij}|^3} d\mathbf{x}_j. \quad (46)$$

There are a number of different cases. If  $l$  and  $m$  are equal, then  $s$  and  $k$  must also be equal, otherwise the integral vanishes. So here we would have three possible contributions to a  $s, k$ -sum, corresponding to the three coordinates that  $s$  and  $k$  can assume. If  $l$  and  $m$  are unequal, then we must either have  $s = l$  and  $k = m$ , or have  $s = m$  and  $k = s$ . So here there are two contributions to a  $s, k$ -sum in this case. Evaluating the integral  $T_{sklm}$  for these cases gives:

$$T_{sklm} = \begin{cases} -\frac{3}{5} & \text{if } l = m \text{ and } s = k = l = m, \\ -\frac{1}{5} & \text{if } l = m \text{ and } s = k, \text{ but } s \neq l, \\ -\frac{1}{5} & \text{if } l \neq m, \text{ and } s = l, k = m \\ & \text{or } s = m, k = l, \\ 0 & \text{in all other cases.} \end{cases} \quad (47)$$

Note that we can pick  $l$  and  $m$  freely when we multiply the Taylor expansion with the term (43) and integrate over it. In particular, we can also use several different choices one after the other and then form a linear combination of the results. This can in fact be used to isolate any of the second derivatives of the Hessian matrix of  $Q_{\alpha\beta}$ . Let us assume for example that we want to calculate the second derivative of  $Q_{\alpha\beta}$  with respect to  $x_0$ . Choosing  $l = m = 0$ , then the three choices  $k = s = 0$ ,  $k = s = 1$  and  $k = s = 2$  all give terms that contribute to the integral over the expansion. These are:

$$2 \int \frac{Q(\mathbf{x}_j) - Q(\mathbf{x}_i)}{|\mathbf{x}_{ij}|^2} (\mathbf{x}_{ij})_0 W_{ij,0} d\mathbf{x}_j = \frac{3}{5} \frac{\partial^2 Q}{\partial x_0^2} + \frac{1}{5} \frac{\partial^2 Q}{\partial x_1^2} + \frac{1}{5} \frac{\partial^2 Q}{\partial x_2^2}. \quad (48)$$

Here  $Q$  is to be understood as  $Q = Q_{\alpha\beta}$  for brevity. Based on this, we can now isolate the desired partial derivative by forming a linear combination:

$$\frac{\partial^2 Q}{\partial x_0^2} = 2 \int \frac{Q(\mathbf{x}_j) - Q(\mathbf{x}_i)}{|\mathbf{x}_{ij}|^2} \times [2(\mathbf{x}_{ij})_0 W_{ij,0} - \frac{1}{2}(\mathbf{x}_{ij})_1 W_{ij,1} - \frac{1}{2}(\mathbf{x}_{ij})_2 W_{ij,2}] d\mathbf{x}_j. \quad (49)$$

In a similar fashion, we can obtain a mixed partial derivative in the following way:

$$\frac{\partial^2 Q}{\partial x_0 \partial x_1} = 2 \int \frac{Q(\mathbf{x}_j) - Q(\mathbf{x}_i)}{|\mathbf{x}_{ij}|^2} \times \left[ \frac{5}{4}(\mathbf{x}_{ij})_0 W_{ij,1} + \frac{5}{4}(\mathbf{x}_{ij})_1 W_{ij,0} \right] d\mathbf{x}_j. \quad (50)$$

Formulae for all other second-order partial derivatives can be obtained from these expressions by cyclic permutation. Also, they are valid for each of the matrix elements  $Q_{\alpha\beta}$ .

Using these results, we can now turn to obtaining an expression for the sum of the second derivatives, as needed in the anisotropic diffusion equation. Based on the above, we can write the desired expression in the compact form:

$$\frac{\partial^2 Q_{\alpha\beta}}{\partial x_\alpha \partial x_\beta} \Big|_{\mathbf{x}_i} = 2 \int \frac{\mathbf{x}_{ij}^T [\tilde{\mathbf{Q}}(\mathbf{x}_j) - \tilde{\mathbf{Q}}(\mathbf{x}_i)] \nabla_i W_{ij}}{|\mathbf{x}_{ij}|^2} d\mathbf{x}_j. \quad (51)$$

Here we defined a new matrix  $\tilde{\mathbf{Q}}$  through the matrix elements of the original matrix  $\mathbf{Q} = (Q_{\alpha\beta})$ , in the following way:

$$\tilde{\mathbf{Q}} = \frac{5}{2} \mathbf{Q} - \frac{1}{2} \text{Tr}(\mathbf{Q}) \mathbf{I}. \quad (52)$$

Inspection of this result highlights one interesting issue that could potentially become a numerical stability problem in certain situations. The matrix  $\tilde{\mathbf{Q}}$  is not guaranteed to correspond to a positive definite quadratic form when it is used in the SPH discretization form of equation (51). If the radiation transfer is very anisotropic, the matrix  $\tilde{\mathbf{Q}}$  can contain negative diagonal elements and thus gives rise to an ‘anti-diffusive’ behaviour in the discretized radiation transfer equation, where radiation is transported from a particle of lower radiation intensity to one with higher radiation intensity. It is not clear right away whether this will lead to numerical stability problems of the radiative diffusion treatment, but it could.

In case this is a problem, one way to avoid it would be to somehow suppress transport of radiation opposite to the direction of the gradient of the radiation intensity between a particle pair. Another way is to add in an isotropic component to  $\tilde{\mathbf{Q}}$  such that

$$\tilde{\mathbf{Q}}^* = \alpha \tilde{\mathbf{Q}} + (1 - \alpha) \frac{\mathbf{I}}{3}. \quad (53)$$

Here the idea is to make  $\tilde{\mathbf{Q}}^*$  slightly more isotropic, such that  $\tilde{\mathbf{Q}}^*$  becomes positive definite again. In order to guarantee this, we need to assign  $\alpha = \frac{2}{5}$ . From equations (52) and (53) we can see that this ‘anisotropy-limited’ matrix is then actually  $\tilde{\mathbf{Q}}^* = \mathbf{Q}$ . One interpretation of this result is that the unmodified matrix  $\mathbf{Q}$  mediates diffusion which is

a mix of 2/5 of the ‘correct’ anisotropic diffusion and 3/5 of isotropic diffusion. In some of our tests we will compare results from both formulations of the matrix. We will refer to  $\tilde{\mathbf{Q}}^*$  as the ‘anisotropy-limited’ tensor and to  $\tilde{\mathbf{Q}}$  as the ‘fully-anisotropic’ tensor.

Note that in the case where  $\mathbf{Q}$  is diagonal and proportional to the identity matrix, equation (51) reduces to the isotropic result for a scalar function derived by Jubelgas et al. (2004) for the thermal conduction problem. The important point about equation (51) is that it involves only a first order derivative of the kernel function. As a result, it can be discretized straightforwardly in the usual SPH way, where the integration is replaced by a sum over all neighboring SPH particles within the kernel volume.

#### 4.3 Discretization of the anisotropic diffusion term in SPH

As we have shown in detail in the previous section, kernel-interpolated second-order derivatives of some tensor  $Q_{\alpha\beta}$  can be obtained as in equation (51) for a suitably defined modified tensor  $\tilde{\mathbf{Q}}$ . Furthermore, we note the identity

$$\frac{\partial}{\partial x} \left( \frac{1}{s} \frac{Q}{\partial y} \right) = \frac{1}{2} \left( \frac{\partial^2}{\partial x \partial y} \frac{Q}{s} - Q \frac{\partial^2}{\partial x \partial y} \frac{1}{s} + \frac{1}{s} \frac{\partial^2 Q}{\partial x \partial y} \right) \quad (54)$$

and thus inserting equation (51) we obtain

$$\frac{\partial}{\partial x_\alpha} \left( \frac{1}{s} \frac{Q_{\alpha\beta}}{\partial x_\beta} \right) = 2 \int \frac{\mathbf{x}_{ij}^T \frac{1}{2} \left( \frac{1}{s_i} + \frac{1}{s_j} \right) [\tilde{\mathbf{Q}}(\mathbf{x}_j) - \tilde{\mathbf{Q}}(\mathbf{x}_i)] \nabla_i W_{ij}}{|\mathbf{x}_{ij}|^2} d\mathbf{x}_j. \quad (55)$$

For our application, let us denote the correspondingly modified Eddington tensor as  $\tilde{h}^{ij}$ . We can then write down an SPH discretization of the diffusion part of the radiation transfer equation. This can be expressed as:

$$\frac{\partial \tilde{n}_\gamma^i}{\partial t} = 2 \sum_j \frac{c}{\kappa_{ij}} \frac{\mathbf{x}_{ij}^T [\tilde{n}_\gamma^j \tilde{\mathbf{h}}_j - \tilde{n}_\gamma^i \tilde{\mathbf{h}}_i] \nabla_i W_{ij}}{\mathbf{x}_{ij}^2} \frac{m_j}{\rho_{ij}}. \quad (56)$$

Here

$$\frac{1}{\kappa_{ij}} = \frac{1}{2} \left[ \frac{1}{\kappa_i} + \frac{1}{\kappa_j} \right] \quad (57)$$

is a symmetric average of the absorption coefficients of the two particles  $i$  and  $j$ , and  $\rho_{ij}$  is a symmetrized density. It is however important to be careful about how exactly the symmetrizations are done in practice, because this can affect the performance of the scheme if there are particles of varying mass. In particular, we would like to use a formulation where the conservation of the number of photons is guaranteed in this case as well. If possible, we would also like to obtain a formulation where the effective coupling matrix is symmetric, because this is a prerequisite for using certain, particularly efficient solution methods from linear algebra, such as the conjugate gradient (CG) method.

The photon conservation property is best analyzed by switching to variables that directly encode the photon number of each particle. Let us define for this purpose the quantity

$$N_i = m_i \tilde{n}_\gamma^i \quad (58)$$

for each particle. The real photon number of a particle is actually  $N_\gamma = n_\gamma m / \rho = m \tilde{n}_\gamma X_H / m_p$ , but we here drop the constant  $X_H / m_p$  in the definition (58), for notational simplicity. Multiplying Eqn. (56) through with  $m_i$  gives now

$$\frac{\partial N_i}{\partial t} = 2 \sum_j \frac{c}{\kappa_{ij} \rho_{ij}} \frac{\mathbf{x}_{ij}^T [m_i N_j \tilde{\mathbf{h}}_j - m_j N_i \tilde{\mathbf{h}}_i] \cdot \nabla_i W_{ij}}{\mathbf{x}_{ij}^2}. \quad (59)$$

Note that we can also write this as

$$\frac{\partial N_i}{\partial t} = \sum_j (w_{ij} N_j - w_{ji} N_i), \quad (60)$$

where

$$w_{ij} \equiv \frac{c}{\kappa_{ij} \rho_{ij}} \frac{\mathbf{x}_{ij}^T m_i \tilde{\mathbf{h}}_j \cdot \nabla_i W_{ij}}{\mathbf{x}_{ij}^2}. \quad (61)$$

From the formulation in equation (60) we easily see that the total photon number,  $\sum_i N_i$ , is conserved, but in general the matrix  $w_{ij}$  is not symmetric. Even though other linear solvers may work, this would prevent us from safely applying the CG scheme to calculate a solution for an backwards-Euler timestep of equation (60), as the required implicit solution involves the inversion of a matrix that linearly depends on  $w_{ij}$  (see below).

To fix this problem, we also symmetrize the mass-weighted Eddington tensor in (60), which results in the following final form of the anisotropic diffusion equation that we use for our numerical implementation:

$$\frac{\partial N_i}{\partial t} = \sum_j w_{ij} (N_j - N_i), \quad (62)$$

where  $w_{ij}$  is now redefined in a symmetric form:

$$w_{ij} \equiv \frac{2 c m_{ij}}{\kappa_{ij} \rho_{ij}} \frac{\mathbf{x}_{ij}^T \tilde{\mathbf{h}}_{ij} \cdot \nabla_i W_{ij}}{\mathbf{x}_{ij}^2}. \quad (63)$$

We may also include the sink term, which yields

$$\frac{\partial N_i}{\partial t} = \sum_j w_{ij} (N_j - N_i) - c \hat{\kappa}_i N_i. \quad (64)$$

This equation is still symmetric and can thus also be treated with the CG method, as we explain in more detail in the next subsection.

#### 4.4 Time integration of the radiative transfer equation

As discussed earlier, we use an operator-split approach for the time integration of the radiation transfer equation, in which we effectively treat the time integration of the source term and that of the transport through anisotropic diffusion and the absorption through the sink terms as separate problems. In fact, we extend the operator-split idea also to the hydrodynamical evolution of the system, i.e. we alternate the timestepping of the diffusion equation with that of the Euler equations that describe the dynamical evolution of the gas. In the following, we first discuss the time integration of the diffusion and sink part, which is the most complicated part in our scheme.

It is well known that explicit time integration schemes of the diffusion equation becomes easily numerically unstable, unless a very small timestep is used. To ensure numerical

stability, we therefore adopt an implicit method, namely the simple ‘backwards Euler’ scheme, which provides sufficient accuracy for the diffusion problem. To advance equation (64) for one timestep, we therefore want to solve the equation

$$N_i^{n+1} = N_i^n + \Delta t \tilde{s}_i m_i + \sum_j \Delta t w_{ij} (N_j^{n+1} - N_i^{n+1}) - \Delta t c \sigma_0 n_{\text{HI}} N_i^{n+1}, \quad (65)$$

where  $N_i^{n+1}$  are the new photon numbers at the end of the timestep, and  $N_i^n$  are the ones at the beginning of step  $n$ . The last term in this equation encodes the photon loss term, which we also integrate implicitly. We note that the source term, on the other hand, can be simply advanced with an explicit Euler step.

The equations (65) are in fact a large, sparsely populated linear system of equations that can be written in the generic form

$$\mathbf{A} \mathbf{x} = \mathbf{b}, \quad (66)$$

where  $\mathbf{A}$  is a coefficient matrix,  $\mathbf{b}$  is a vector of known values and  $\mathbf{x}$  is a vector of unknown values. For our application, the components of vector  $\mathbf{b}$  are  $b_i = N_i^n + \Delta t \tilde{s}_i m_i$ , and the matrix elements are given by

$$A_{ij} = \delta_{ij} \left( 1 + \sum_k \Delta t w_{ik} + \Delta t c \sigma_0 n_{\text{HI}} \right) - \Delta t w_{ij}, \quad (67)$$

where the indexes  $i$  and  $j$  run over all the SPH particles. The solution vector of the linear problem defines the new photon numbers at the end of the step,  $x_i = N_i^{n+1}$ .

There are many different approaches for solving linear systems of equations, but the huge size of the matrix  $\mathbf{A}$  in our problem (which is equal to the particle number squared) makes many standard approaches that rely on storing the whole matrix  $\mathbf{A}$  impractical. Fortunately, the matrix  $\mathbf{A}$  is only sparsely populated because in each row only approximately  $\sim N_{\text{sph}}$  elements are non-zero, those that describe the coupling of a particle to its neighbors. Sparse systems of this type can often be solved well with iterative schemes. We use such an iterative scheme in our work, the conjugate gradient (CG) method.

The conjugate gradient approach applies successive corrections to a trial solution that is used as a starting point. With every iteration, the solution becomes better. Since the corrections added in each of the steps are all orthogonal to each other, the rate of convergence of this method is often quite high, this is why we think it is a promising iteration scheme for the problem at hand. For reference, a derivation of the well-known CG method is given in Appendix B and Appendix C. However, a prerequisite for the applicability of the conjugate gradient method is that the matrix  $\mathbf{A}$  is positive definite and symmetric. The symmetry is evident from our formulation and the matrix is positive definite since  $w_{ij} \geq 0$ , and thus  $\sum_{ij} x_i A_{ij} x_j \geq 0 \forall x_i$ .

To find a solution for the new photon number field, we iterate with the CG scheme until the difference between two successive approximations to  $\mathbf{x}$  has dropped to a small percentage of  $|\mathbf{x}|$ . Note that the expensive parts in the calculation of one iteration are the matrix-vector multiplications. For each particle, they reduce to sums over all of its SPH neighbors, which is equivalent to an ordinary SPH loop, similar in computational cost to, e.g., the SPH density estima-



tion. Since in our parallel code some of the SPH neighbours of a particle can be stored on other processors, this step also involves communication.

In practice, we start the iteration with the current photon distribution for  $\mathbf{x}$ , which is usually a fairly good starting point, since the expected solution for the photon distribution does not differ significantly from the previous state, except in the vicinity of the sources. In the absence of a radiation field we set the vector to zero. The closer the guessed values for the vector  $\mathbf{x}$  are to the solution, the faster the algorithm converges. One could also start from a random photon distribution, which will not affect the solution, but will slow down the algorithm and is therefore not a desirable choice. The number of iterations required to reach convergence depends on the condition number of the matrix  $\mathbf{A}$ , where the condition number is defined as  $\lambda_{\max}/\lambda_{\min}$ , the ratio of the largest to the smallest eigenvalue of the matrix. A large condition number slows down the convergence rate of iterative solvers of linear systems of equations. However, the number of required iterations can be reduced by *pre-conditioning* the matrix  $\mathbf{A}$ . For this purpose we employ the simple Jacobi preconditioner. More specifically, we modify our matrix equation as follows,

$$\mathbf{C}^{-1} \mathbf{A} \mathbf{x} = \mathbf{C}^{-1} \mathbf{b}, \quad (68)$$

where the matrix  $\mathbf{C}$  is the Jacobi preconditioning matrix. It is defined as

$$C_{ij} = A_{ii} \delta_{ij}, \quad (69)$$

and has the rather simple inverse form

$$C_{ij}^{-1} = \frac{\delta_{ij}}{A_{ii}}. \quad (70)$$

Applying the Jacobi preconditioner to the matrix  $\mathbf{A}$  basically means to divide the matrix  $\mathbf{A}$  by its diagonal, which is simple to implement and to parallelize. While the associated reduction of the condition number improves the convergence speed, it would be desirable to find still better preconditioners that are more effective in this respect.

#### 4.5 Implicit time integration of the chemical network

The chemical network we need to solve is described by equation (35). Even though it contains only a simple time derivative, the numerical integration can be rather tricky because very large changes in the number of ionising photons can *suddenly* occur from timestep to timestep. A stable integration with a simple explicit scheme therefore requires a very small timestep, of the order of  $10^{-5}$  the typical dynamical timestep of the simulation. This would make the solution of the chemical network very expensive, and it is highly desirable to find another method that speeds up the computation.

To this end we use an implicit scheme for the evolution of the chemical network. Our variant of this approach discretizes equation (35) in time as follows (here the upper index  $n$  denotes the integration time step):

$$\frac{\tilde{n}_{\text{HII}}^n - \tilde{n}_{\text{HII}}^{n-1}}{\Delta t} = c \sigma_0 n_{\text{H}} \tilde{n}_{\text{HI}}^n \tilde{n}_{\gamma}^n - \alpha n_{\text{H}} (\tilde{n}_{\text{HII}}^n)^2, \quad (71)$$

where we have substituted  $\tilde{n}_e = \tilde{n}_{\text{HII}}$ . This quadratic equation is easy to solve. We have found this scheme to be quite accurate and robust even for moderately large timesteps.

#### 4.6 Photoheating and cooling with a multi-frequency scheme

Since our code tracks monochromatic radiation, we need to provide a multi-frequency description that allows photoheating of the irradiated gas. Such approaches have already been introduced by Mihalas & Weibel Mihalas (1984) and are often used in the literature (e.g. Aubert & Teyssier 2008). The frequency spectrum of the source is approximated by a black body spectrum, which allows the use of a frequency independent photoionisation cross-section  $\tilde{\sigma}$  defined as

$$\tilde{\sigma} = \int_0^\infty d\nu \frac{4\pi\sigma_\nu J_\nu}{h\nu} \times \left( \int_0^\infty d\nu \frac{4\pi J_\nu}{h\nu} \right)^{-1}. \quad (72)$$

Similarly, a frequency averaged photon energy  $\tilde{\epsilon}$  (above the hydrogen ionisation energy) can be defined. Thus the hydrogen photoheating rate from equation (8) can be approximated by

$$\Gamma = n_{\text{HI}} c \tilde{\epsilon} \tilde{\sigma} n_{\gamma}, \quad (73)$$

where  $c$  is the speed of light and  $n_{\gamma}$  is the number density of ionising photons.

In order to evolve the temperature of the gas correctly we consider cooling processes such as recombination cooling, collisional ionisation cooling, collisional excitation cooling and Bremsstrahlung cooling. All rates have been adopted from Cen (1992) and are summarized in Appendix A. As a combination of heating and cooling terms the temperature of each particle is then evolved as follows

$$T^{n+1} = T^n + \Delta t \frac{2}{3k_{\text{B}} n_{\text{H}}} [\Gamma - \Lambda], \quad (74)$$

where the upper index  $n$  denotes the timestep of the simulation,  $k_{\text{B}}$  is the Boltzmann constant,  $n_{\text{H}}$  is the hydrogen number density,  $\Gamma$  is the heating rate and  $\Lambda$  is total cooling rate, evaluated for the new temperature at the end of the step.

#### 4.7 The source terms

As given in equation (34), the source term in the RT equation is  $\tilde{s}_{\gamma}$  in our formulation. This represents the number of photons emitted per unit time and per hydrogen atom. In our cosmological applications we usually want to represent this term by the stars that have formed in the simulation. To more accurately account for the short-lived massive stars, we can also use star-forming SPH particles as sources, converting their instantaneous star formation rates into an ionising luminosity. Alternatively, we can also consider harder sources like Active Galactic Nuclei (AGN), if they are followed in the simulation. The time integration of the source function is unproblematic, and can be done with a simple explicit scheme on the dynamical timestep of the simulation. We only need to assign the source luminosities in a conservative fashion to the nearest SPH particles, provided they are not already gas particles anyway.

In some of our test problems considered in Section 5, the source term is prescribed as a certain number  $\dot{N}_{\gamma}$  of ionising photons per second, independent of the mass of the source. In this case we have

$$\tilde{s}_{\gamma} = \frac{\dot{N}_{\gamma}}{n_{\text{H}} V} = \dot{N}_{\gamma} \frac{m_p}{m}, \quad (75)$$

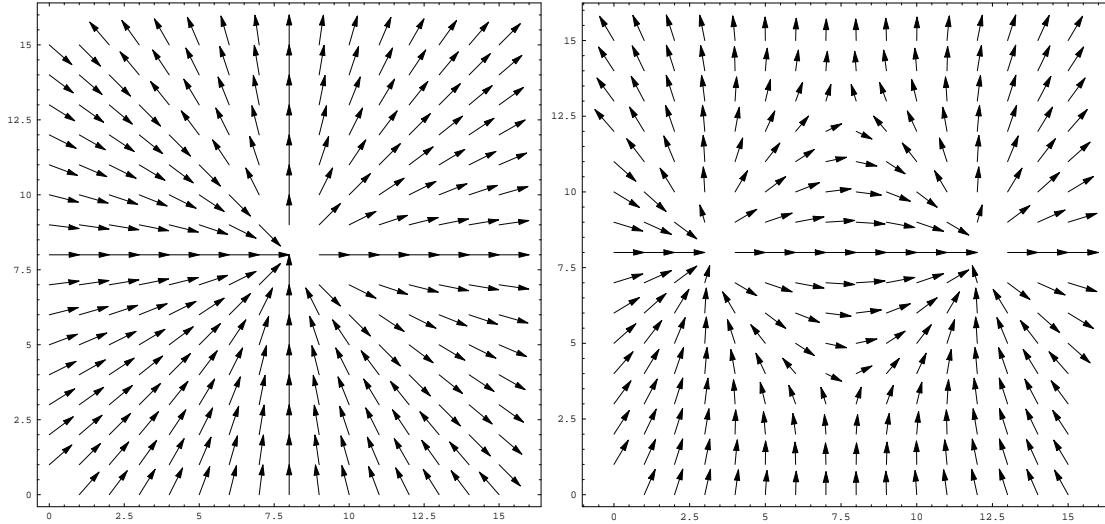


**Figure 1.** Eigenvectors of the Eddington tensor for a single source (left panel), and for two sources (right panel), calculated with our tree-code extensions of the GADGET-3 code. Both vector fields match the expectations. Note that the directions of the vectors can be turned  $180^\circ$  without affecting the direction of the transport of radiation, an effect due to the symmetric nature of the Eddington tensor.

where  $V = m/\rho$  is a measure of the volume of the SPH particle with mass  $m$  that hosts the source. If we choose to distribute the source function to more than one particle, we use the ‘scatter’ approach. In this case the source function has the form

$$\tilde{s}_\gamma = \dot{N}_\gamma \sum_j \frac{m_j}{\rho_j} W(r) \frac{m_p}{m_j}, \quad (76)$$

where the sum is over the SPH neighbors of the emitting particle.

#### 4.8 Eddington tensor calculation

An important quantity in our formulation of the RT problem are the local Eddington tensors, which we estimate based on an optically thin approximation, as defined by equations (20) and (21). The  $1/r^2$  dependence of the contribution of each source suggests a calculation method similar to that of gravity – via a hierarchical tree algorithm. To this end we extend the gravitational tree code in GADGET-3 with additional data structures. For each node of the tree, we also calculate the total luminosity and the luminosity-weighted centre-of-mass. Depending on whether we consider the star particles as sources, the star-formation rate of gas particles, or also black hole particles, this can involve different types of particles.

The individual elements of the Eddington tensor are then computed by walking the tree in a way exactly analogous to the procedure for calculating gravitational forces. If a tree node appears under a small enough angle as seen from the point of interest, all its sources can be represented by the total luminosity of the node. Otherwise, the tree node is opened, and the daughter nodes are considered in turn. As a result, we obtain a multipole approximation to the local radiation pressure tensor, with a typical accuracy of  $\sim 1\%$ , provided a similar node-opening threshold value is used as for collisionless gravitational dynamics. However, since for the Eddington tensor only the direction of the radiation

pressure tensor ultimately matters, the final accuracy of the Eddington tensor is even better, and more than sufficient for our purposes. A very important property of this calculational method is that its overall speed is essentially independent of the number of sources that are present since the calculation is done simultaneously with the tree-walk that computes gravity, and involves only few additional floating point operations. This is quite different from the widely employed ray-tracing or Monte-Carlo schemes for radiation transfer, where the calculation cost may scale linearly with the number of sources.

As an example, Figure 1 shows the eigenvectors of the Eddington tensor for two different source configurations, calculated with our modified version of the GADGET-3 code. The left panel is for a single source. The vectors point radially outward or inward from the source, as expected. Note that the directions of the vectors can be turned by  $180^\circ$  without changing the radiation transport, because the tensor is symmetric. The panel on the right hand side shows the vector field around two sources, in the plane of the stars. The field is a dipole in this case and matches the expectations well.

#### 4.9 Flux limited diffusion

If  $n_\gamma$  is the density of photons, then the maximum photon flux  $f$  that can occur is limited by the speed of light to  $f = cn_\gamma$ . This physical limit for the possible photon flux can in principle be violated under certain conditions when the diffusive approximation to the photon flux,

$$f^j = -\frac{1}{\kappa_\nu} \frac{1}{a} \frac{\partial n_\gamma h^{ij}}{\partial x^i}, \quad (77)$$

is used. In treatments of radiative transfer in the isotropic diffusion approximation one therefore often invokes so-called flux limiters that are designed to enforce the condition

$$f \leq cn_\gamma \quad (78)$$

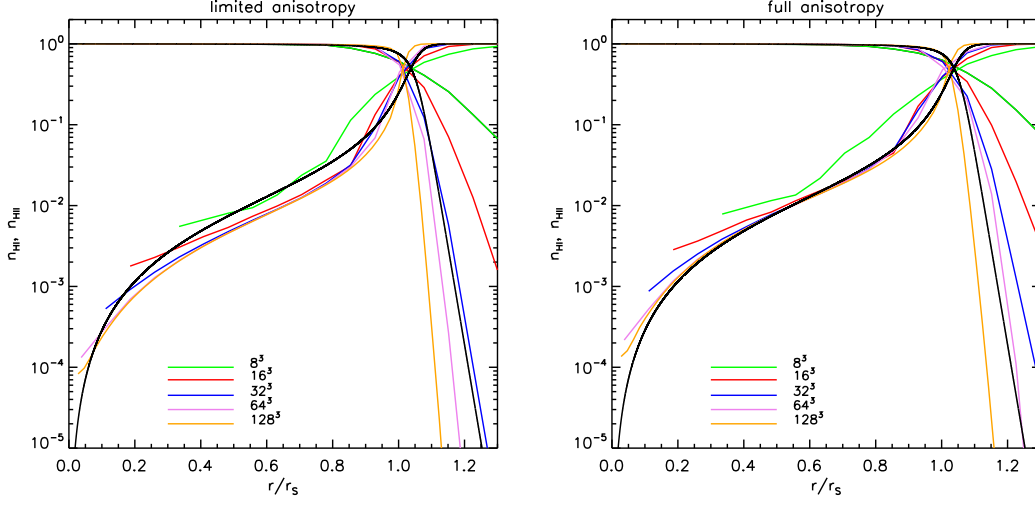


**Figure 2.** Resolution comparison of spherically averaged ionised and neutral fractions as a function of radial distance from the source, normalized by the Strömgren radius  $r_s$ . Results are shown for an anisotropy-limited (left panel) and fully anisotropic (right panel) Eddington tensor formulation at time  $t = 500 \text{ Myr} \sim 4t_{\text{rec}}$ . The compared resolutions are  $8^3$ ,  $16^3$ ,  $32^3$ ,  $64^3$  and  $128^3$  particles. The black lines show the analytical solution, integrated radially outward from the source as in equation (87). In both formulations the accuracy clearly increases with resolution and saturates when the highest number of particles is reached. In all cases, the final Strömgren radius agrees with the analytical predictions. The anisotropy-limited Eddington tensor formalism gives very accurate predictions for the ionised fraction in the regions outside the Strömgren radius ( $r > r_s$ ), but fails to give a correct value for the inner parts of the ionised regions. The fully anisotropic Eddington tensor formalism, however, predicts accurate values in both regions.

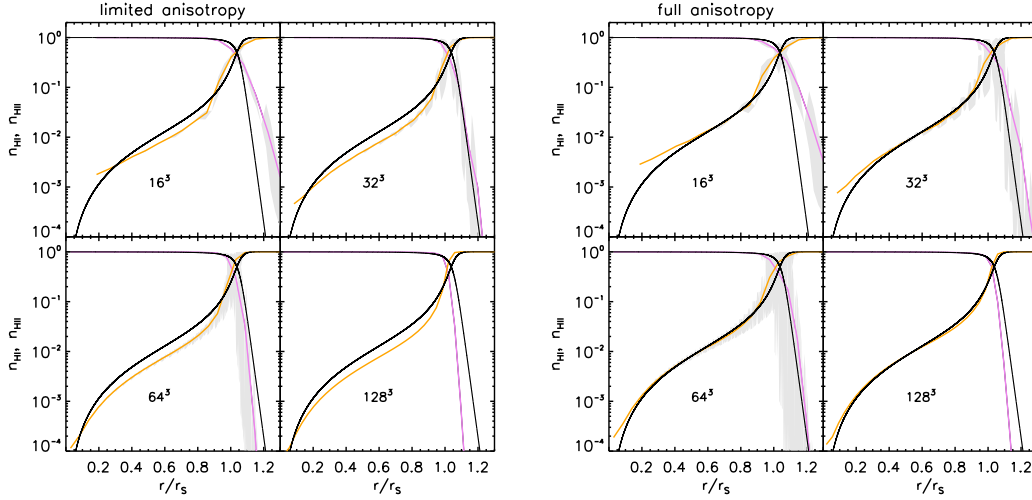


**Figure 3.** Resolution comparison of the scatter (grey areas) of the spherically averaged ionised and neutral fraction as function of radial distance from the source, normalized by the Strömgren radius  $r_s$ . Results are shown for an anisotropy-limited (left panel) and fully anisotropic (right panel) Eddington tensor formulation at time  $t = 500 \text{ Myr} \sim 4t_{\text{rec}}$ . The compared resolutions are  $16^3$ ,  $32^3$ ,  $64^3$  and  $128^3$  particles. The black lines show the analytical solution, integrated radially outward from the source as in equation (87). The orange lines show the spherically averaged neutral fraction and the violet lines the spherically averaged ionised fraction. The range of the scatter does not change significantly with resolution, since it is due to the intrinsic diffusive nature of SPH and the inaccuracies of the SPH density estimate. The highest resolution simulation has no scatter due to the high accuracy of the density estimates. The scatter in the fully anisotropic Eddington tensor formalism is larger due to the larger anisotropy in the diffusion terms of the RT equation.

by damping the estimated flux when needed.

In our anisotropic diffusion treatment, we have also implemented an optional limiter that serves the same purpose. We observe the maximum flux constraint with the help of a parameter  $R$ , which is a function of the gradient of the photon density

$$R \equiv \frac{|\nabla n_\gamma|}{\kappa n_\gamma}. \quad (79)$$

We then define a flux limiter of the form

$$\lambda(R) = \frac{1 + 0.1R}{1 + 0.1R + 0.01R^2}, \quad (80)$$

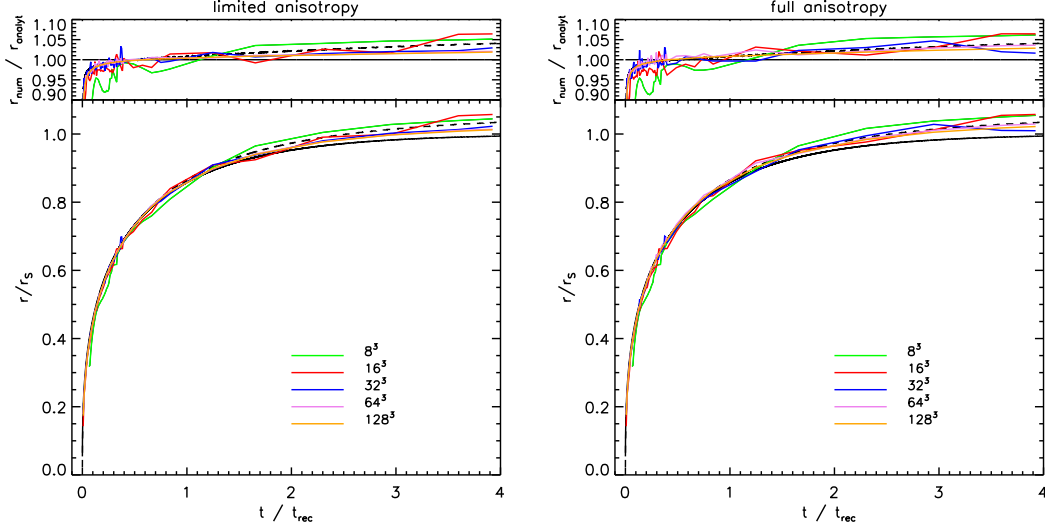


**Figure 4.** I-front expansion for an anisotropy-limited (left panel) and a fully anisotropic (right panel) Eddington tensor formulation with  $16^3$ ,  $32^3$ ,  $64^3$  and  $128^3$  particles. The dashed line is the exact solution obtained from equation (87) and the solid one as obtained from equation (83). Both results agree very well with the analytical predictions, but the fully anisotropic Eddington tensor formulation shows better results and smaller relative error for the I-front position.

where  $\lambda(R) \rightarrow 0$  as  $R \rightarrow \infty$ . The detailed form of the analytic expression used for the flux limiter is arbitrary as long as it ensures a smooth transition between the two limiting states. We have chosen this form since it is widely used in other numerical RT codes, for example, a similar version is used by Whitehouse & Bate (2004). The flux limiter  $\lambda$  is then introduced into the diffusion part of equation (34) as follows:

$$\frac{\partial \tilde{n}_\gamma}{\partial t} = c \frac{\partial}{\partial x_j} \left( \frac{\lambda}{\kappa} \frac{\partial \tilde{n}_\gamma h^{ij}}{\partial x_i} \right) - c \kappa \tilde{n}_\gamma + \tilde{s}_\gamma. \quad (81)$$

However, we note that superluminal propagation of photons is usually not a problem in the ionisation problems we are interested in. Here the speed of the ionisation fronts is not limited by the speed of light, but rather by the luminosity of the sources and the density of the absorbing medium. Nevertheless, the flux limiter can also be usefully employed as a means to control the behavior of the ionisation front (I-front) propagation in dense media. Due to the specific dependence of the  $R$  parameter, the photon propagation can effectively be limited in high-density regions, where the intensity gradient becomes very large.

#### 4.10 Notes on the performance of the code

An important consideration in the development of RT codes is the calculational cost of the implemented scheme, as this determines whether the method is sufficiently fast to allow a coupling with hydrodynamic simulation codes. It is difficult to make general statements about the computational cost of our new RT scheme as this depends strongly on the particular physical problem that it is applied to. Arguably of most interest is a comparison of the speed of the method to other parts of the simulation code when applied to the problem of cosmological structure formation with a self-consistent treatment of cosmic reionisation. We here report approximate numbers for the speed of our new method

in this situation, based on work in preparation that studies this problem.

First we note that in our implementation, when gravity is also integrated, the computation of the Eddington tensor incurs negligible costs, since it is done together with the gravity. Therefore, we find that in our implementation the increase of the computational cost with respect to the other relevant code modules (gravity, SPH density and SPH hydrodynamical forces) is primarily a function of the number of iterations required at each timestep to construct the implicit solution of the anisotropic diffusion equation. One iteration is approximately as costly as one SPH hydro computation, and the average number of iterations required ranges from typically 10 up to 200 in the most extreme cases. However, the RT equation is integrated only on a relatively coarse timestep, whereas the hydrodynamics is done also for many more smaller sub-steps. This reduces the effective cost of the whole RT calculation to several times the total cost of the hydrodynamics calculations. In practice, we measure a slow-down of the simulation code by a factor of order of 2 to 5 when the radiative transfer is included. While this is non-negligible, it does not seriously impact the ability to carry out large cosmological simulations. We also note that further optimizations in the radiative transfer algorithms, perhaps through an improved pre-conditioner, may reduce the cost of the RT calculation in the future.

## 5 TESTING THE CODE

In the following we present several basic tests for our new radiative transfer code. Where possible, we compare our results with analytical solutions or with results from other simulations (from the RT code comparison study by Iliev et al. 2006). In section 5.1 we discuss our results for the classic test of the isothermal expansion of an ionised sphere in a homogeneous and static density field. In section 5.1.1 we

study the effects of different timesteps on the accuracy of our simulations, while in section 5.1.2 we evolve two nearby sources with interacting ionised spheres. Then in section 5.2 we repeat the single ionised sphere expansion test, but this time allowing the temperature to evolve. In section 5.3 we present a shadowing test, where a dense clump is placed in the way of a plane-parallel I-front. Finally, in section 5.4 we evolve the radiation transport in a static cosmological density field.

### 5.1 Isothermal ionised sphere expansion

The expansion of an I-front in a static, homogeneous and isothermal gas is the only problem in radiation hydrodynamics that has a known analytical solution and is therefore the most widely used test for RT codes. A monochromatic source emits steadily  $\dot{N}_\gamma$  photons with energy  $h\nu = 13.6$  eV per second into an initially neutral medium with constant gas density  $n_H$ . Then the Strömngren radius, at which the ionised sphere around the source has reached its maximum radius, is defined as

$$r_S = \left( \frac{3\dot{N}_\gamma}{4\pi\alpha_B n_H^2} \right)^{1/3}, \quad (82)$$

where  $\alpha_B$  is the recombination coefficient. This radius is obtained by balancing the number of emitted photons by the number of photons lost due to recombinations along a given line of sight. If we assume that the I-front is infinitely thin, i.e. there is a discontinuity in the ionisation fraction, then the expansion of the Strömngren radius can be solved analytically and the I-front radius  $r_I$  is given by

$$r_I = r_S [1 - \exp(-t/t_{\text{rec}})]^{1/3}, \quad (83)$$

where

$$t_{\text{rec}} = \frac{1}{n_H \alpha_B} \quad (84)$$

is the recombination time and  $\alpha_B$  is the recombination coefficient.

The neutral and ionised fraction as a function of radius of the stable Strömngren sphere can be calculated analytically (e.g. Osterbrock & Ferland 2006) from the equation

$$\frac{\tilde{n}_{\text{HI}}(r)}{4\pi r^2} \int d\nu \dot{N}_\gamma(\nu) e^{-\tau_\nu(r)} \sigma_\nu = \tilde{n}_{\text{HII}}^2(r) n_H \alpha_B, \quad (85)$$

where  $\tilde{n}_{\text{HI}}$  is the neutral fraction,  $\tilde{n}_{\text{HII}}$  is the ionised fraction and

$$\tau_\nu(r) = n_H \sigma_\nu \int_0^r dr' \tilde{n}_{\text{HI}}(r'). \quad (86)$$

Moreover, considering spherical symmetry and a point source we can solve analytically for the photon density radial profile  $n_\gamma(r)$ , yielding

$$n_\gamma(r) = \frac{1}{c} \frac{\dot{N}_\gamma}{4\pi r^2} \exp \left\{ - \int_0^r \kappa(r') dr' \right\}. \quad (87)$$

From this we obtain ionised fraction profiles  $\tilde{n}_{\text{HII}}(r)$  for the whole evolution time.

The Strömngren radius obtained by direct integration of equation (85) differs from the one obtained from equation (82) because it does not approximate the ionised region as a

sphere with constant, but with varying ionised fraction. We compare our results with both analytical solutions.

For definiteness, we follow the expansion of the ionised sphere around a source that emits  $\dot{N}_\gamma = 5 \times 10^{48}$  photons  $\text{s}^{-1}$ . The surrounding hydrogen number density is  $n_H = 10^{-3} \text{ cm}^{-3}$  at a temperature of  $T = 10^4$  K. At this temperature, the case B recombination coefficient is  $\alpha_B = 2.59 \times 10^{-13} \text{ cm}^3 \text{ s}^{-1}$ . Given these parameters, the recombination time is  $t_{\text{rec}} = 125.127$  Myr and the expected Strömngren radius is  $r_S = 5.38$  kpc. We impose periodic boundary conditions in order to make sure that the density field is effectively infinite and uniform. We note that this does not affect our RT calculation since the Eddington tensor is computed non-periodically.

We present results from the fully-anisotropic and the anisotropy-limited Eddington tensor formalism simulations by comparing first the final state of the ionised sphere and then the evolution of the I-front. Figure 2 shows the spherically averaged ionised and neutral fraction as a function of radial distance from the source, normalized by the Strömngren radius  $r_S$ , at time  $t = 500$  Myr  $\sim 4 t_{\text{rec}}$ . In this case we compare the resolution effects on the accuracy of our numerical predictions by using simulations with  $8^3$ ,  $16^3$ ,  $32^3$ ,  $64^3$  and  $128^3$  particles, corresponding to mean spatial resolutions of 2.0 kpc, 1.0 kpc, 0.5 kpc and 0.25 kpc. In both formalisms the accuracy increases with resolution and the profiles converge for the higher resolutions. We also note that the anisotropy-limited Eddington tensor formalism gives very accurate predictions for the ionised fraction in the regions outside the Strömngren radius ( $r > r_S$ ), but fails to give correct values in the inner parts of the ionised sphere. The fully anisotropic Eddington tensor formalism, on the other hand, predicts the ionisation state in both regions quite accurately.

We compare also the scatter of the ionised and neutral fraction profiles. Figure 3 shows the scatter (gray areas) of the spherically averaged ionised and neutral fraction profiles for four different resolutions ( $16^3$ ,  $32^3$ ,  $64^3$  and  $128^3$  particles) at the end of the I-front expansion. All results agree well with the analytical radius of the Strömngren sphere. The range of the scatter does not change significantly with resolution, since it is due to the intrinsic diffusive nature of SPH and the inaccuracies of the SPH density estimate. This means that we obtain a density scatter of about 0.01% and thus introduce fluctuations in the gas density, which result in fluctuations in the hydrogen densities of the SPH particles and thus of the ionised and neutral fractions. The SPH density scatter in the  $128^3$  particle simulation is zero (thanks to the use of a Cartesian grid – but note that in real-world dynamical applications some density scatter is unavoidable) and thus there is no scatter in the ionised and neutral fractions. Moreover, the scatter in the fully anisotropic Eddington tensor formalism simulations is larger than in the other formalism simulations due to the larger retained anisotropy in the diffusion term of the RT equation.

The evolution of the I-front expansion is shown in Figure 4, comparing the two formalisms at different resolutions. The results from both formalisms agree very well with the analytical predictions and the accuracy increases with resolution. The fully anisotropic Eddington tensor formalism simulations show better results and smaller relative error for the I-front position. In both formalisms the error stays

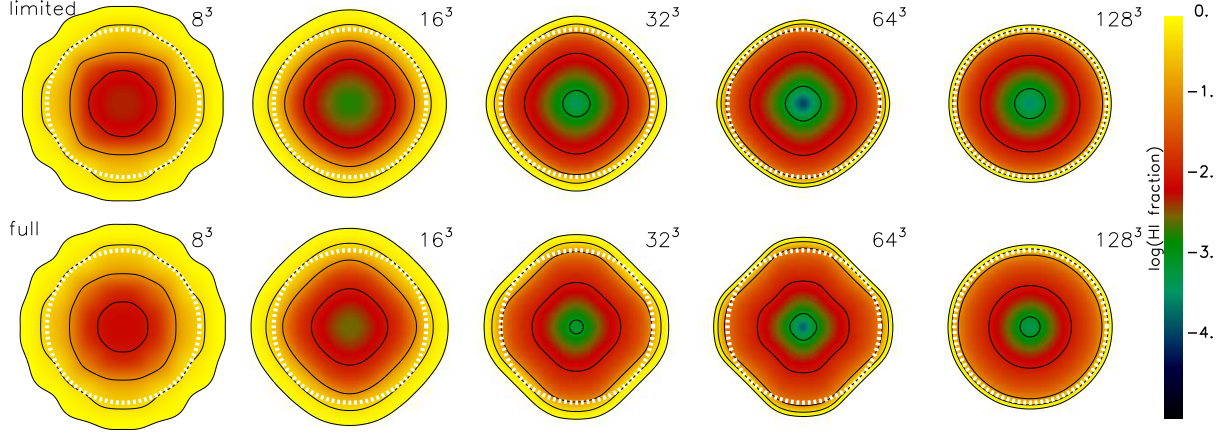


**Figure 5.** Slices of the neutral fraction through the ionised sphere at the position of the source. The upper row shows the results from the anisotropy-limited Eddington tensor formulation and the lower row from the fully anisotropic Eddington tensor formalism. Five different resolutions are compared:  $8^3$ ,  $16^3$ ,  $32^3$ ,  $64^3$  and  $128^3$  particles. The contours mark neutral fractions of  $\bar{n}_{\text{HI}} = 0.9, 0.5, 0.1, 0.01$  and  $0.001$ . The white circles give the radius of the Strömgren sphere. The geometrical distribution of the SPH particles affects the shape of the ionised sphere. The spheres are elongated in the  $x$ - and  $y$ -direction of the Cartesian grid, where the particle spacing is smaller and the SPH-kernel interpolant leads to slightly different couplings as in diagonal directions. This effect is stronger for the anisotropic Eddington tensor formulation.

within 5% of the analytical solution and traces the analytical result obtained by direct integration of equation (87).

However, we note that the geometrical distribution of the SPH particles we used in our simulations introduces slight deviations from perfect sphericity into the shape of the ionised region. This reflects the Cartesian grid of particles used for these tests, an effect that can be clearly seen in the shapes of the ionised regions displayed in Figure 5. The spheres are elongated in the  $x$ - and  $y$ -directions of the Cartesian grid, where the particle spacing is smaller and the SPH-kernel interpolant weights the nearest neighbours slightly differently than in off-axis directions. This discreteness effect is stronger for the anisotropic Eddington tensor formulation.

Considering all our results that compare the limited and fully anisotropic Eddington tensor formalisms, we use in all our further tests and simulations only the fully anisotropic formulation because it shows more accurate results. It turns out that this formulation is also robust, i.e. it does not show stability problems due to its ‘anti-diffusive’ terms when used in conjunction with an implicit solver, at least we have not experienced such problems in our test calculations.

### 5.1.1 Timestep comparison

In order to test the accuracy of our RT scheme we perform simulations of  $64^3$  particle resolution with different fixed timesteps:  $\Delta t = 0.05, 0.5, 5$  and  $50$  Myr. Applying the von Neumann stability criterion for an explicit integration of the diffusion part of our RT equation (19), we find a bound of the timestep equal to

$$\Delta t \leq \frac{1}{2} \frac{\kappa(\Delta x)^2}{c}, \quad (88)$$

where  $\Delta x$  is the mean spatial resolution,  $c$  is the speed of light and  $\kappa = n_{\text{HI}} \sigma$  is the absorption coefficient. At the I-front the assumed neutral fraction is  $\bar{n}_{\text{HI}} = 0.5$  and thus the absorption coefficient is  $\kappa = 3.15 \times 10^{-21} \text{ cm}^{-1}$ , resulting in

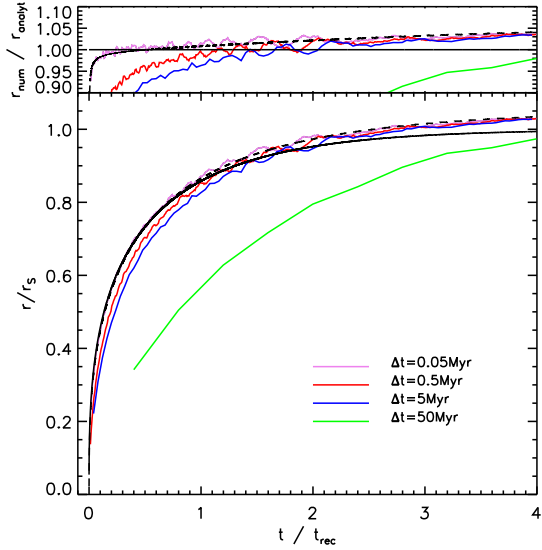


**Figure 6.** I-front expansion as a function of the recombination time. Results are shown for four different simulation timesteps:  $\Delta t = 0.05, 0.5, 5$  and  $50$  Myr. The dashed line is the exact solution obtained from equation (87) and the solid one is obtained from equation (83). The smallest timestep simulation agrees very well with the analytical solution. As the timestep increases, the results in the early phases of the expansion become more inaccurate. However, after about two recombination times, the I-front radius catches up with the analytical solution. The simulation with timestep  $\Delta t = 50$  Myr is very inaccurate, but in the end of the expansion the I-front radius is still within 5% of the analytical solution.

an upper limit for the timestep  $\Delta t \leq 10^{-3}$  Myr. However, this limit on the timestep is only a reference point for our results. Because we use an implicit scheme that is stable for all timestep sizes, we are fortunately not bound by this timestep limit and can in principle use much larger timesteps, subject



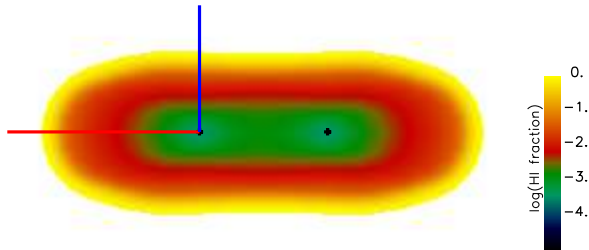


**Figure 7.** Ionised fraction in a plane of two equally luminous sources. The positions of the sources (8 kpc apart) are marked with black crosses. The snapshot is taken at time  $t = 500$  Myr, when the expansion of the ionised regions has stopped, and the region where the Strömgren spheres overlap is approximately 3 kpc wide. There is a clear elongation along the axis connecting the two sources, as also described by Gnedin & Abel (2001). Figure 8 shows the evolution of the I-front along the aligned (red) and perpendicular (blue) directions with respect to the axis through the sources.

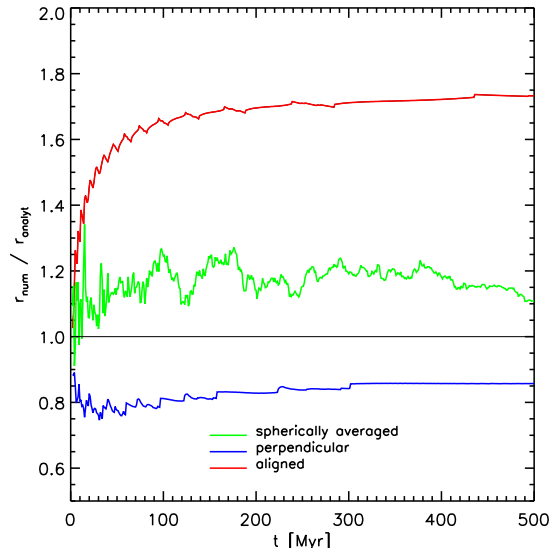
only to the condition that the final accuracy reached is still acceptable.

We compare results for our simulations with the four different timestep sizes in Figure 6. The smallest timestep that we use is ten times as big as the analytical upper limit for an explicit scheme, yet its results agree perfectly with the analytical solution. For the other simulations the timestep sizes increase progressively by factors of 10, and the numerical results start to deviate from the analytical calculation. The changes are largest in the early phase of the I-front expansion. As the source “suddenly” switches on, very small time steps are needed in order to achieve good accuracy in the beginning, where the gradients in the photon density are very large. But later, after a couple of recombination times, the numerical results approach the analytical solution even for coarse timesteps and follow it until the expansion of the I-front ends. The  $\Delta t = 50$  Myr simulation is initially very inaccurate, but note that its Strömgren radius is still within 5% of the analytical result. Therefore, our method manages to essentially produce correct Strömgren radii of the ionised spheres for all considered timesteps.

### 5.1.2 Two nearby sources

In our next test we follow the expansion of ionised regions around two nearby sources, where we expect to see inaccuracies due to the optically thin assumption used for estimating the Eddington tensors. Both sources emit  $N_\gamma = 5 \times 10^{48}$  photons  $\text{s}^{-1}$  and are 8 kpc away from each other. The number density of the surrounding static and uniform hydrogen gas is  $n_H = 10^{-3} \text{ cm}^{-3}$ , at a temperature of  $T = 10^4 \text{ K}$ . From tests conducted by Gnedin & Abel (2001) we expect that the ionised regions are not spherical, but rather elongated along the axis through the sources. This effect results from the calculation of the Eddington tensor, whose values along the symmetry axis are estimated high and boost the diffusion in this direction, while reducing it in the perpendicular direction.

In Figure 7, we show the neutral fraction for this test in a slice in the plane of the sources, taken at time  $t = 500$  Myr when the expansion of the regions has stopped. The expected elongated shape of the ionised regions is clearly visible. In



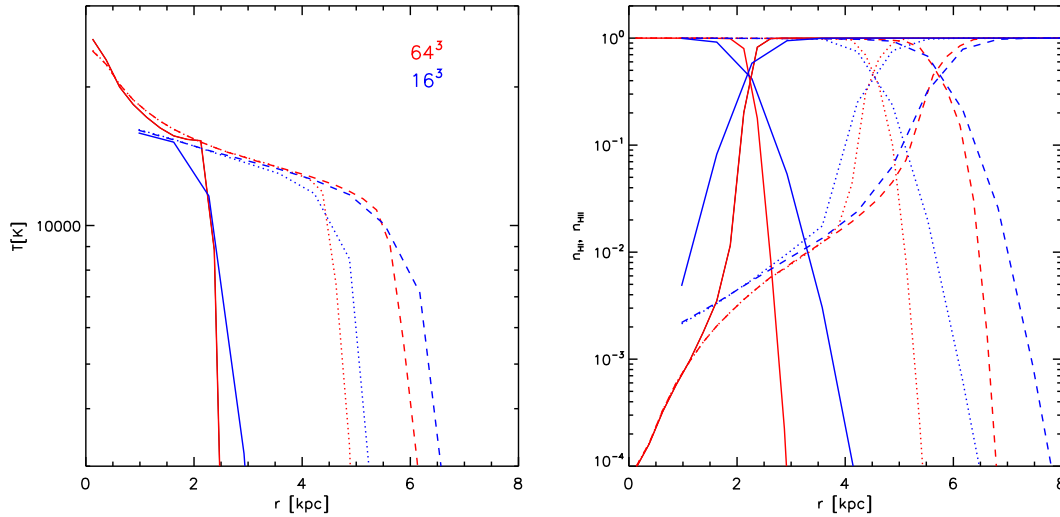
**Figure 8.** I-front expansion around a source in a double system, normalized by the analytical solution from equation (83), as a function of time. The red line is the I-front in the direction aligned with the two sources and the blue line is for the orthogonal direction. The green line shows the spherically averaged I-front position. As observed by Gnedin & Abel (2001), the ionised spheres are elongated along the axis of the two sources and compressed in the perpendicular direction. The spherically averaged I-front position is within 20% of the analytical expectation.

Figure 8 we show the time evolution of three characteristic radii of the expanding ionised regions: one radius is measured in a direction aligned with the axis through the sources, one is measured perpendicular to it, and the third is a spherically averaged radius. We note that we do not expect the radii to match the analytical prediction from equation (83) exactly since the approximations there are valid only for a single ionised region expansion, but we here use the obtained value to compare the expansion of the ionised regions around two nearby sources. As expected, the aligned radius is always larger than the analytical result, while the perpendicular radius is smaller. However, the spherically averaged radius of the expanding region stays within 20% of the analytical value. We conclude that the optically thin approximation to estimate Eddington tensors can in certain situations introduce errors in the shapes of ionised bubbles, but these errors should be quite moderate or negligible in situations where the Eddington tensor is dominated by a bright nearby source, which is probably generic in many scenarios for cosmological reionisation.

### 5.2 Ionised sphere expansion with varying temperature

In this test we use the same setup as in section 5.1, but we initialize the gas temperature with  $T_0 = 10^2 \text{ K}$  and let it evolve due to the coupling to the radiation field. We furthermore approximate the recombination coefficient  $\alpha_B$  with

$$\alpha_B(T) = 2.59 \times 10^{-13} \left( \frac{T}{10^4 \text{ K}} \right)^{-0.7} \text{ cm}^3 \text{ s}^{-1}, \quad (89)$$



**Figure 9.** Time evolution of temperature (left panel) and ionised and neutral fraction (right panel) profiles of an expanding ionised sphere for two different resolutions:  $16^3$  (blue) and  $64^3$  (red) particles. Results at times  $t = 10, 100$  and  $500$  Myr are shown in solid, dotted and dashed lines, respectively. The temperature profiles inside the ionised sphere converge for both resolutions at all times. The position of the I-front agrees well for both resolutions at all times.

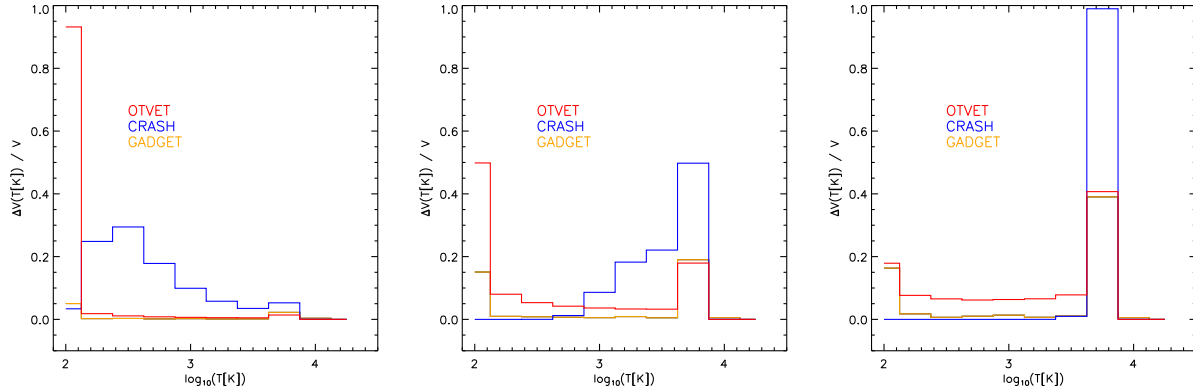


**Figure 10.** Volume fraction of the temperature for a comparison between CRASH, OTVET and GADGET at three different times  $t = 10, 100$  and  $500$  Myr (left to right). The results of GADGET and OTVET are comparable, but CRASH has a harder spectral distribution and employs multiple frequency bins and thus gives slightly different results. Differences between GADGET and OTVET may also be due to different resolutions (OTVET has  $0.05$  kpc, while for GADGET  $\sim 0.25$  kpc).

and assume a black body spectrum of temperature  $10^5$  K for the source, setting the parameters from equation (73) to  $\tilde{\sigma} = 1.63 \times 10^{-18} \text{ cm}^2$  and  $\tilde{\epsilon} = 29.65 \text{ eV}$ . Then we evolve equation (74) for every particle, at every time step, considering photoheating, recombination cooling, collisional ionisation cooling, collisional excitation cooling and Bremsstrahlung cooling. In this way we test a realistic expansion of an ionised sphere around a single source.

We test our scheme with two different resolutions:  $16^3$  and  $64^3$  particles. The time evolution of the temperature profile in both tests is shown in the left panel of Figure 9. The temperature close to the source rises to approximately  $2 \times 10^4$  K and then drops down to  $10^2$  K outside the ionised region. From left to right, the profiles are shown at three different times:  $t = 10, 100$ , and  $500$  Myr. The results from the simulations converge inside the ionised sphere. Outside the ionised region the low resolution simulation produces,

as expected, a smaller slope of the temperature drop further from the ionised sphere radius. In the right panel of Figure 9, we compare the neutral and ionised fractions at the same times. Both resolutions converge at the radius of the ionised sphere.

In order to verify our results we compare them with results obtained with the codes CRASH (Maselli et al. 2003) and OTVET (Gnedin & Abel 2001), as summarized by Iliev et al. (2006) in the RT Code Comparison Project. In Figure 10, we show a comparison of the volume fraction of the temperature and in Figure 11 we present a comparison of the ionised volume fractions, at three different times:  $t = 10, 100$ , and  $500$  Myr. The temperature volume fractions are all somewhat different due to the very different heating schemes employed. The results of GADGET and OTVET are comparable, but CRASH uses a harder spectral distribution and multiple frequency bins and thus gives different results.



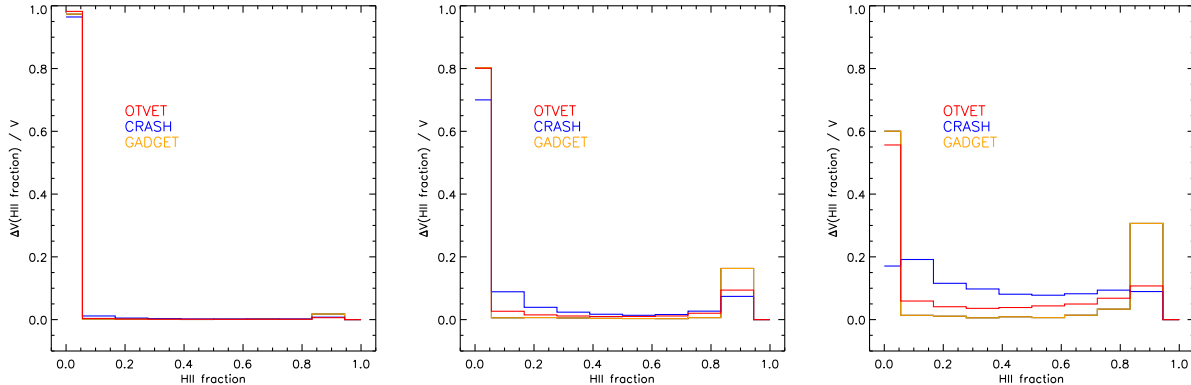


**Figure 11.** Volume fraction of the ionised fraction in a comparison between CRASH, OTVET and GADGET for three different times  $t = 10, 100$  and  $500$  Myr (left to right). With increasing time, GADGET produces larger strongly ionised volume and smaller intermediately ionised volume than the other codes, mirrored in the larger gradient of the ionised fraction that it produces. These deviations are likely due to different source spectra treatments, temperature structures of the ionised spheres, and different numerical resolutions.

With increasing time GADGET produces a larger strongly ionised volume, and smaller intermediately ionised volume fraction than the other codes, which is also mirrored in the larger gradient of the ionised fraction that it produces. These differences are due to the different treatments of the source spectra that the codes employ, which are in general difficult to compare. Deviations might also be due to the different temperature structures of the ionised spheres and the different resolutions of the codes (OTVET and CRASH used  $0.05$  kpc, GADGET only  $\sim 0.25$  kpc).

### 5.3 Shadowing by a dense clump

As a further test problem, we consider the interaction of a plane-parallel front of ionising photons with a uniform dense cylinder of neutral gas. The setup of our problem consists of a box with dimensions  $(x, y, z) = (40 \text{ kpc}, 10 \text{ kpc}, 20 \text{ kpc})$ . One side of which (the  $xy$ -plane) is aligned with a plane of stars that produce the ionising photons. A dense cylinder of gas is located  $5$  kpc from this sheet-like source and has a radius  $r_C = 2.5$  kpc. The axis of the cylinder is oriented parallel to the  $z$ -axis of the box. The particle resolution is  $(N_x, N_y, N_z) = (256, 64, 8)$ . The hydrogen number density in the cylinder is  $10^5$  times the surrounding density of  $n_H = 10^{-3} \text{ cm}^{-3}$ . There are  $512$  stars and each of them emits  $\dot{N}_\gamma = 1.2 \times 10^{48} \text{ photons s}^{-1}$ .

We first present results obtained with an Eddington tensor that mimics a plane-parallel I-front, of the form

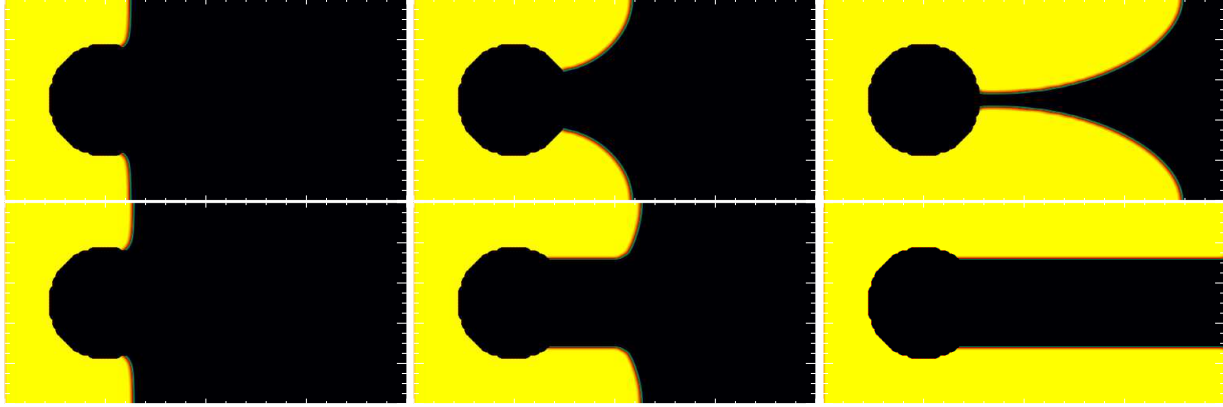
$$\tilde{\mathbf{h}} = \begin{pmatrix} 1 & 0 & 0 \\ 0 & 0 & 0 \\ 0 & 0 & 0 \end{pmatrix}, \quad (90)$$

which represents photon transport only in the  $x$ -direction. We also consider two other cases where the Eddington tensor is calculated differently. In the first case we use the OTVET approximation, where the tensor is computed assuming all gas is optically thin. In the second case we account for the fact that the dense clump is optically thick by enforcing that no radiation is transported into the shadowed region. We achieve this by setting the Eddington tensor in the shadowed area to zero, such that the product  $h^{ij} J_\nu$  vanishes. Note that

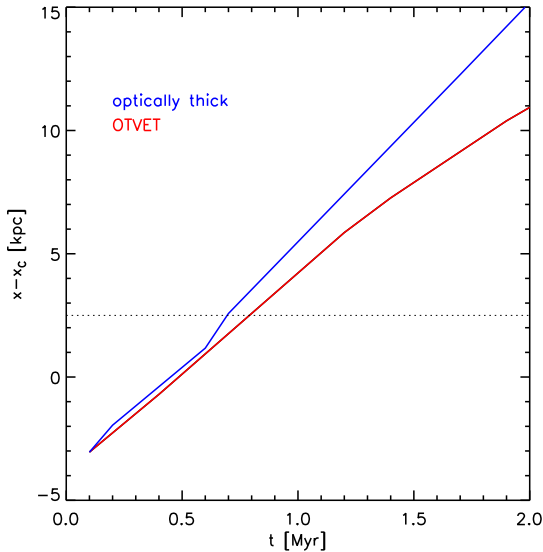
for a vanishing radiation pressure tensor, the trace condition for the Eddington tensor needs not to be fulfilled. This second case is only meant to produce the expected solution with a sharp shadow.

Figure 12 shows the ionised fraction in a cut through the simulation volume, in the plane  $z = z_{\text{box}}/2$ , at three different times:  $t = 0.5, 1$ , and  $2$  Myr. In the case of the OTVET approximation (first row), the dense cylinder fails to produce a sharp shadow. Instead, the radiation also diffuses around the obstacle, and is propagated eventually also in directions different from the  $x$ -direction, albeit more slowly. However, if we account for the fact that the dense clump is optically thick (second row), a clear and sharp shadow is produced, as expected. In Figure 13, we show the position of the I-front with respect to the centre of the dense clump as a function of time. It is clear that the I-front moves faster in the case where the Eddington tensor is approximated closer to the analytical case, i.e. it is zero in the shadow area.

The inability to create a sharp shadow is a limitation of the OTVET approximation implemented in SPH, as we have shown above. This limitation of codes using a moment method together with an OTVET approximation has already been noted by several groups, e.g. Gnedin & Abel (2001); Aubert & Teyssier (2008). It appears that despite our attempts to fully account for the anisotropic diffusion, the diffusion operator we have derived remains quite diffusive in SPH. This is simply a consequence of the non-vanishing coupling between particles with separation vectors not perfectly aligned with the direction of radiation propagation (here the  $x$ -axis). Unfortunately, this deficiency may also have other detrimental effects besides just slowing down the expansion of the I-front itself. We acknowledge that this can be an important limitation of our scheme for certain applications, especially when shielding is common and shadowing is important. Nevertheless, this limitation can influence the morphology of the reionisation, but properties such as redshift and duration of the process, as well as temperature evolution of the gas and the radiation field, should still be accurate.



**Figure 12.** Ionised fraction (yellow) in a slice through the middle of the simulation box. Time increases from left to right and the three different columns of snapshots are taken at  $t = 0.5, 1$ , and  $2$  Myr. In the upper row the Eddington tensor has been approximated with the OTVET scheme. In the second row the Eddington tensor has been set to zero in the shadowed region, given that the dense clump is optically thick, which should yield the correct result. The optically thin Eddington tensor approximation fails to produce a sharp shadow since radiation diffuses away from the plane-parallel front direction. In the optically thick approximation, however, a sharp shadow is obtained, implying that the failure of our method to produce a sharp shadow can also be blamed on using a non-vanishing Eddington tensor in the shadowed region.



**Figure 13.** Position of the I-front, relative to the centre of the dense clump, as a function of time. The I-front moves faster in the case where the Eddington tensor is computed accounting for the optically thick clump (blue line). In the case where the OTVET scheme is used (red line), the I-front expands slower. The dashed line shows the position at the end of the clump, where the difference between the expansion rates begins to grow.

#### 5.4 Static cosmological density field

In our final and most demanding test calculation we follow hydrogen ionisation in a realistic cosmological density field, which is taken to be static for simplicity. In order to compare our results with those of the cosmological radiative transfer comparison project (Iliev et al. 2006) we use the same cosmological box parameters and assign sources in the same way. The box with size  $0.5 h^{-1}$  comoving Mpc is evolved with a standard  $\Lambda$ CDM model with the following cosmological parameters:  $\Omega_0 = 0.27$ ,  $\Omega_b = 0.043$ ,  $h = 0.7$ ,

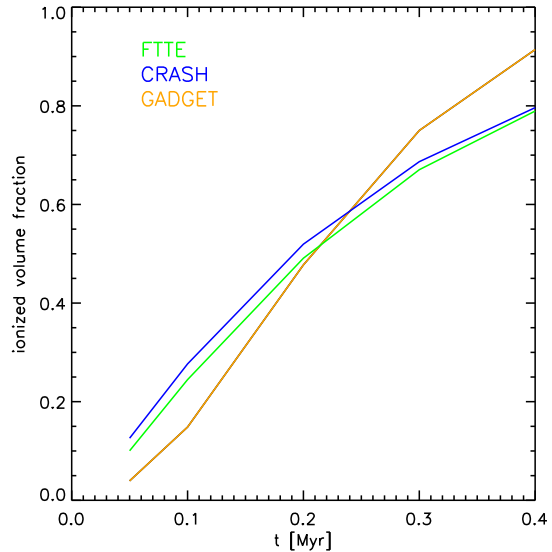


**Figure 14.** Time evolution of the volume-averaged ionised fraction in the whole simulation box. In comparison to CRASH (blue) and FTTE (green), GADGET (orange) produces lower ionised fractions at earlier times and higher ionised fractions at later times. The overall trend in the increase of the ionised fraction is the same, and the speed of ionisation first accelerates and then decelerates. Differences between our results and the ones from the Comparison Project are in part also due to differences in the initial conditions, as we had to transform the grid-based density field to an SPH realization.

until redshift  $z = 9$ . The density field at this point is considered for our further analysis.

The source distribution is determined by finding halos within the simulation box with a FOF algorithm and then assigning sources to the 16 most massive ones. The photon luminosity of the sources is

$$\dot{N}_\gamma = f_\gamma \frac{M\Omega_b}{\Omega_0 m_p t_s}, \quad (91)$$

where  $M$  is the total halo mass,  $t_s = 3 \text{ Myr}$  is the lifetime of the source,  $m_p$  is the proton mass and  $f_\gamma = 250$  is the number of emitted photons per atom during the lifetime of the source. We find that the total source luminosity in our simulated box agrees well with the one from Iliev et al. (2006). For simplicity we also set the initial temperature of the gas to 100 K throughout the whole box.

We found that simply mapping the grid cells onto a Cartesian mesh of SPH particles with different masses introduces large noise into our RT calculation, due to the large variations in the mass of neighbouring particles. It is therefore not straightforward to translate the mesh-based data of the code comparison project into an equivalent SPH realization, and we therefore needed to create our own initial conditions. We note that simple methods to create an equal particle mass SPH realization from the given grid cells, e.g. through random sampling, tend to introduce large amounts of Poisson noise and wash out extrema in the density field.

The evolution of the total volume-averaged ionised fraction in the box is very similar for GADGET and the Comparison Project codes, as shown in Figure 14. In the beginning of the simulation the total ionised fraction rises rapidly and then the increase decelerates. GADGET produces an overall lower ionised fraction until approximately  $t = 0.2 \text{ Myr}$  and higher one at later times. This mismatch is in part certainly caused by the morphological differences in the initial conditions that introduce different clumping properties of matter and therefore different I-front expansion histories. We recall that the true solution of the problem is unknown. Given the non-linearity of the system, the differences in detail of the initial conditions and cooling rates, and the fact that we compare fundamentally different RT schemes, the agreement that we obtain is actually very good.

To illustrate the spatial distribution of the ionised fraction and the temperature of the gas we show in Figure 15 slices through the simulation volume at  $z = 0.7z_{\text{box}}$  (through the largest group) at three different times  $t = 0.05, 0.2$  and  $0.4 \text{ Myr}$ . The upper row shows contours of the neutral fraction plotted over a density field, the second row shows a map of the neutral fraction and the third row shows a map of the temperature of the gas. The dense regions trap the I-front and thus produce sharp gradients of the radiation density. In the under-dense regions ionisation is more effective and the I-front is extended. Even though the ionised regions are mostly uniform, traces of the dense structures that are less ionised can be seen near the front-trapping points. As shown in the contour maps, the I-fronts are broader in the low density regions and thinner in the high density regions. The temperature in the ionised regions reaches several  $10^4 \text{ K}$  and is uniform. It remains unchanged outside, where no photons are present.

We further compare the volume fraction of the temperature and the ionised fraction from GADGET, CRASH and FTTE in Figures 16 and 17, at three different times  $t = 0.05, 0.2$ , and  $0.4 \text{ Myr}$ . The temperature volume fractions do not match particularly well due to the different photoheating mechanisms that GADGET, CRASH and FTTE use, but they find a similar maximum temperature. The volume fractions of the ionised fraction for GADGET, CRASH and FTTE have similar shapes. GADGET, in contrast to the other codes, produces less intermediately ionised gas. However, overall the histograms are in a reasonably good agreement with each

other, suggesting that our moment-based scheme is quite capable in describing the reionisation process and produces results of similar accuracy as other established radiative transfer codes.

## 6 SUMMARY AND CONCLUSIONS

We have presented a novel method for solving the radiative transfer equations within SPH, which is based on moments of the radiative transfer equation that are closed with a variable Eddington tensor. The radiation transport effectively becomes an anisotropic diffusion problem in this formulation. We have developed a new discretization scheme for anisotropic diffusion in SPH together with an implicit time integration method which for the first time allows a calculation of such anisotropic diffusion in SPH. Together with a scheme to estimate Eddington tensors based on the optically thin approximation, this yields a very fast approximate treatment of radiative transfer that can be used in dynamical SPH calculations.

We have implemented our method into the cosmological simulation code GADGET-3 and presented several test problems where we varied the initial conditions and different numerical parameters to investigate the accuracy of the method. Our test results agree in general very well with analytical predictions and data from other simulations, except that the long-term evolution of sharp geometric shadows is clearly not followed accurately. While this clearly limits the range of applicability of the method, we expect that the method can still provide reasonably accurate results for problems where shadowing is comparatively unimportant, such as cosmological reionisation, where the SPH-based variable Eddington tensor approach can be competitive with other techniques. However, our method has two important strengths not shared by most other techniques: It can easily cope with an arbitrary number of sources since its speed is essentially independent of the number of sources, and furthermore, it is fast enough to be included into a cosmological simulation code where radiative transfer is calculated on-the-fly together with the ordinary dynamics. This is especially promising for future calculations of galaxy formation and reionisation that we want to carry out with our new code.

The epoch of reionisation is an important and extremely interesting process in the evolution of the Universe. There is already very important observational evidence that constrains reionisation, but few precise statements about the onset, duration, and end of reionisation can be made at this point. The situation will likely change in the near future through upcoming observations, ranging from new CMB observations with PLANCK, to 21cm tomography at high redshift with radio telescopes such as LOFAR. In the meantime, we heavily rely on cosmological simulations to advance our understanding of the reionisation process.

However, the simulations run so far leave many questions still unanswered, and their lack of self-consistency with the actual dynamics and the rapidly evolving source population may have introduced sizable inaccuracies. It is therefore highly desirable to have new numerical techniques that do not rely on solving the radiative transfer equation in a post-processing mode by treating only individual snapshot

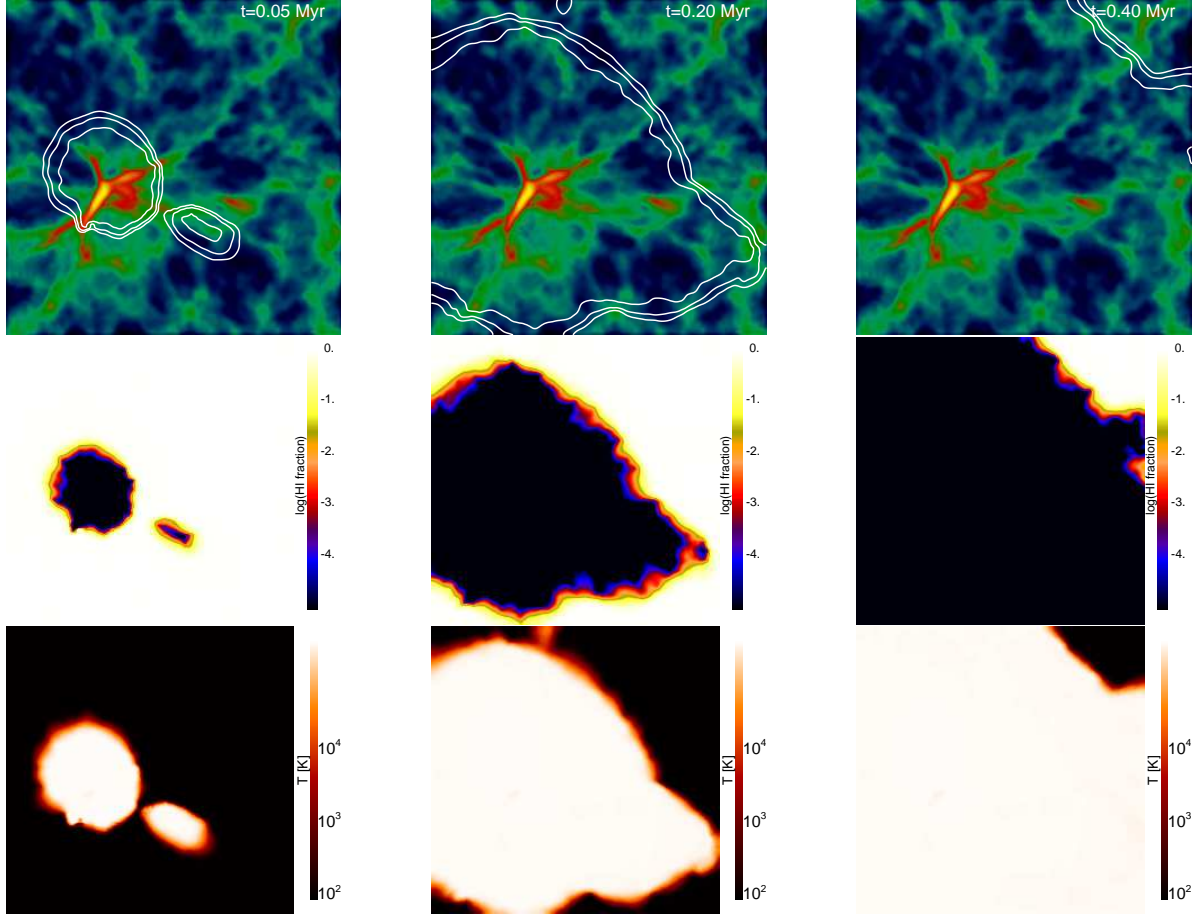


**Figure 15.** The upper row shows contours of neutral fractions equal to 0.01, 0.5 and 0.9 in a slice through the simulation volume at  $z = 0.7z_{\text{box}}$ , through the largest group. The snapshots are taken at times  $t = 0.05, 0.2$  and  $0.4$  Myr (left to right). The background shows a slice of the density distribution. The ionised regions expand with time as the I-front is trapped at high density regions and extends into low density regions. The second row shows the neutral fraction in the same slice. The ionised regions are uniform with some substructure visible near the front-trapping regions, where the I-front is not as diffuse as in low density regions. The third row shows the temperature distribution in the slice. The temperature in the ionised regions reaches several  $10^4$  K and remains uniform outside these regions.

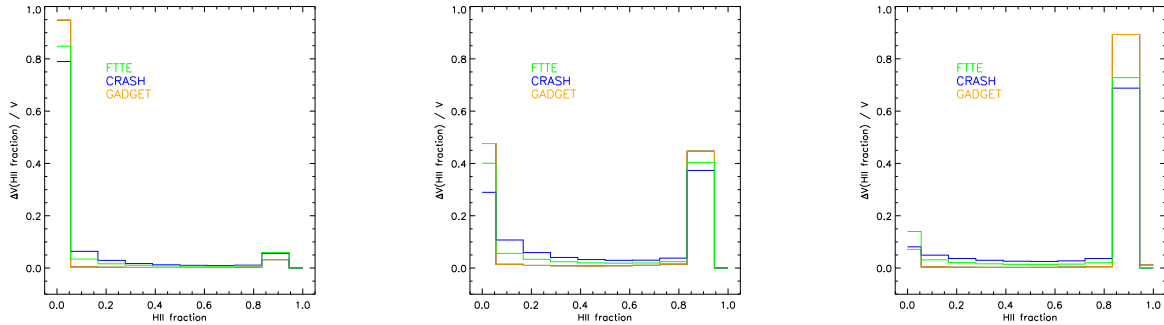


**Figure 16.** Volume fraction of the ionised fraction at three different times  $t = 0.05, 0.2$ , and  $0.4$  Myr (left to right). Results from GADGET are compared with results from CRASH and FTTE from Iliev et al. (2006). All codes match in the shape of the histograms, but GADGET gives a lower intermediately ionised fraction.

files from simulations. Rather, accurate calculations should account for radiative transfer ‘on-the-fly’, so that the gas properties are affected simultaneously by gravity and radiation. Our new method promises to be an important step in this direction. In future work, one of our most important goals is therefore to carry out high-resolution simulations of

structure formation where the build-up of stellar and quasar sources in galaxies is followed self-consistently with the radiation field, allowing us to make more accurate predictions for the temporal evolution of reionisation, and the topology of reionised regions as a function of time.

All tests problems we have presented in this thesis agree

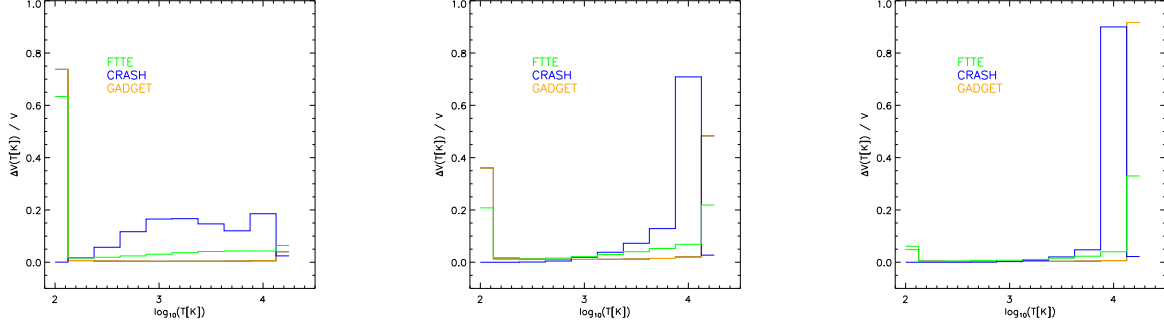


**Figure 17.** Volume fraction of the temperature at three different times  $t = 0.05, 0.2$  and  $0.4$  Myr (left to right). Results from GADGET are compared with results from CRASH and FTTE from Iliev et al. (2006). All codes produce different histograms. FTTE and GADGET agree better with each other at later evolution times. CRASH produces higher temperatures due to its use of a different spectral distribution.

well with theoretical predictions or results obtained with other radiative transfer codes. We should be able to obtain a realistic and accurate temperature evolution of the Universe during reionisation, which is important for setting the ‘cosmic equation of state’ that regulates the absorption seen as Lyman- $\alpha$  forest in the spectra of distant quasars. Finally, we plan to include the photoionisation of other elements besides hydrogen, most importantly of helium. Helium reionisation probably happened sometime at redshift  $z \sim 2 - 4$ , where it may have left a sizable imprint in the temperature evolution of the intergalactic medium. Surprisingly, recent observations suggest that the temperature-density relation of the IGM may be inverted (Bolton et al. 2008), which could be caused by radiative transfer effects related to helium reionisation. Whether this is indeed possible can only be clarified with simulations. Studying this question with our new methods would therefore be particularly timely.

## ACKNOWLEDGEMENTS

This research was supported by the DFG cluster of excellence Origin and Structure of the Universe (www.universe-cluster.de).

## APPENDIX A: COOLING RATES

Here we present all cooling rates that we have used in our simulations with temperature evolution (Section 5.2). The rates have been obtained from Cen (1992) and are given in  $\text{erg cm}^{-3} \text{s}^{-1}$ .

(i) Recombination cooling rate

$$\Lambda_r = 8.7 \times 10^{-27} \sqrt{T} \left( \frac{T}{10^3} \right)^{-0.2} \left/ \left[ 1 + \left( \frac{T}{10^6} \right)^{0.7} \right] \right. n_e n_{\text{HI}}, \quad (\text{A1})$$

(ii) Collisional ionisation cooling rate

$$\Lambda_{ci} = 1.27 \times 10^{-21} \sqrt{T} \left( 1 + \sqrt{\frac{T}{10^5}} \right) \exp \left( \frac{-157809.1}{T} \right) n_e n_{\text{HI}}, \quad (\text{A2})$$

(iii) Collisional excitation cooling rate

$$\Lambda_{ce} = 7.5 \times 10^{-19} \left( 1 + \sqrt{\frac{T}{10^5}} \right)^{-1} \exp \left( \frac{-118348}{T} \right) n_e n_{\text{HI}}, \quad (\text{A3})$$

(iv) Bremsstrahlung cooling rate

$$\Lambda_B = 1.42 \times 10^{-27} g_{\text{ff}} \sqrt{T} n_e n_{\text{HI}}, \quad (\text{A4})$$

where  $g_{\text{ff}} = 1.3$  is the Gaunt factor.

## APPENDIX B: METHOD OF STEEPEST DESCENT

In this Appendix, we give a derivation of the CG technique for solving linear problems, which we employ in our implicit time integration scheme of the anisotropic diffusion problem. As the CG scheme is closely related to the method of steepest descent, we start with an explanation of this more general technique, and then specialize to the CG method.

The method of steepest descent is a scheme to solve a linear system of equations given by  $\mathbf{A}\mathbf{x} = \mathbf{b}$ . The idea is to obtain the solution as the minimum of the quadratic form

$$f(\mathbf{x}) = \frac{1}{2} \mathbf{x}^T \mathbf{A} \mathbf{x} - \mathbf{b}^T \mathbf{x}, \quad (\text{B1})$$

such that

$$f'(\mathbf{x}) = \frac{1}{2} \mathbf{A}^T \mathbf{x} + \frac{1}{2} \mathbf{A} \mathbf{x} - \mathbf{b}. \quad (\text{B2})$$

This equation reduces to

$$f'(\mathbf{x}) = \mathbf{A} \mathbf{x} - \mathbf{b} \quad (\text{B3})$$

if  $\mathbf{A}$  is symmetric and positive definite, i.e. if  $\mathbf{x}^T \mathbf{A} \mathbf{x} > 0$  for all  $\mathbf{x} \neq 0$ .

We now consider an iteration scheme that tries to find the solution  $\mathbf{x}$ . As we take steps, we choose the direction of the next step in the direction in which the quadratic form  $f$  decreases most rapidly, which is in the direction opposite to the gradient  $f'(\mathbf{x})$ . Therefore, the next step should be proportional to  $-f'(\mathbf{x}_{(i)}) = \mathbf{b} - \mathbf{A}\mathbf{x}_{(i)}$ . Here the index  $i$  denotes the number of the step we take towards the correct value of  $\mathbf{x}$ . Let us denote the difference between the numerical and the exact solution as  $\mathbf{e}_{(i)} = \mathbf{x}_{(i)} - \mathbf{x}$ , and the residual as  $\mathbf{r}_{(i)} = \mathbf{b} - \mathbf{A}\mathbf{x}_{(i)} = -f'(\mathbf{x}_{(i)})$ . Therefore, the next step taken is given by  $\mathbf{x}_{(1)} = \mathbf{x}_{(0)} + \alpha \mathbf{r}_{(0)}$ . The optimum value of  $\alpha$  is chosen such that the directional derivative  $\frac{d}{d\alpha} f(\mathbf{x}_{(1)})$  equals 0, i.e. the vectors  $f'(\mathbf{x}_{(1)})$  and  $\mathbf{r}_{(0)}$  should be chosen orthogonal:

$$\frac{d}{d\alpha} f(\mathbf{x}_{(1)}) = f'(\mathbf{x}_{(1)})^T \frac{d}{d\alpha} \mathbf{x}_{(1)} = f'(\mathbf{x}_{(1)})^T \mathbf{r}_{(0)} = 0 \quad (\text{B4})$$

We further notice that  $f'(\mathbf{x}_{(1)}) = -\mathbf{r}_{(1)}$  and therefore

$$\begin{aligned} \mathbf{r}_{(1)}^T \mathbf{r}_{(0)} &= 0 \\ (\mathbf{b} - \mathbf{A}\mathbf{x}_{(1)})^T \mathbf{r}_{(0)} &= 0 \\ (\mathbf{b} - \mathbf{A}(\mathbf{x}_{(0)} + \alpha \mathbf{r}_{(0)}))^T \mathbf{r}_{(0)} &= 0 \\ (\mathbf{b} - \mathbf{A}\mathbf{x}_{(0)})^T \mathbf{r}_{(0)} - \alpha (\mathbf{A}\mathbf{r}_{(0)})^T \mathbf{r}_{(0)} &= 0 \\ (\mathbf{b} - \mathbf{A}\mathbf{x}_{(0)})^T \mathbf{r}_{(0)} &= \alpha (\mathbf{A}\mathbf{r}_{(0)})^T \mathbf{r}_{(0)} \\ \mathbf{r}_{(0)}^T \mathbf{r}_{(0)} &= \alpha \mathbf{r}_{(0)}^T (\mathbf{A}\mathbf{r}_{(0)}) \\ \alpha &= \frac{\mathbf{r}_{(0)}^T \mathbf{r}_{(0)}}{\mathbf{r}_{(0)}^T \mathbf{A}\mathbf{r}_{(0)}} \end{aligned}$$

Finally, putting it all together, the method of steepest descent is as follows

$$\mathbf{r}_{(i)} = \mathbf{b} - \mathbf{A}\mathbf{x}_{(i)} \quad (\text{B5})$$

$$\alpha_{(i)} = \frac{\mathbf{r}_{(i)}^T \mathbf{r}_{(i)}}{\mathbf{r}_{(i)}^T \mathbf{A}\mathbf{r}_{(i)}} \quad (\text{B6})$$

$$\mathbf{x}_{(i+1)} = \mathbf{x}_{(i)} + \alpha_{(i)} \mathbf{r}_{(i)} \quad (\text{B7})$$

$$\mathbf{r}_{(i+1)} = \mathbf{r}_{(i)} - \alpha_{(i)} \mathbf{A}\mathbf{r}_{(i)} \quad (\text{B8})$$

### APPENDIX C: CONJUGATE GRADIENT METHOD

In the method of steepest descent the value of  $\mathbf{x}$  is determined via successively adding the search directions  $\mathbf{r}_{(i)}$ . Let us define the set of directions  $\{\mathbf{d}_{(i)}\}$  as the search directions for the CG method, such that  $\mathbf{x}_{(i+1)} = \mathbf{x}_{(i)} + \alpha_{(i)} \mathbf{d}_{(i)}$  and  $\mathbf{r}_{(i+1)} = \mathbf{r}_{(i)} - \alpha_{(i)} \mathbf{A}\mathbf{d}_{(i)}$ . We further require that the vectors  $\{\mathbf{d}_{(i)}\}$  are  $\mathbf{A}$ -conjugate, i.e.  $\mathbf{d}_{(i)} \mathbf{A} \mathbf{d}_{(j)} = 0$ , which means

$$\mathbf{d}_{(i+1)} = \mathbf{r}_{(i+1)} + \sum_{k=0}^i \beta_{ik} \mathbf{d}_{(k)}. \quad (\text{C1})$$

Using Gram-Schmidt orthogonalization, the coefficients  $\beta_{ik}$  are found to be

$$\beta_{ik} = \begin{cases} \frac{1}{\alpha_{(i-1)}} \frac{\mathbf{r}_{(i)}^T \mathbf{r}_{(i)}}{\mathbf{d}_{(i-1)}^T \mathbf{A} \mathbf{d}_{(i-1)}} & \text{for } i = k + 1 \\ 0 & \text{for } i > k + 1 \end{cases} \quad (\text{C2})$$

Thus

$$\beta_{(i)} \equiv \beta_{i,i-1} = \frac{\mathbf{r}_{(i)}^T \mathbf{r}_{(i)}}{\mathbf{r}_{(i-1)}^T \mathbf{r}_{(i-1)}}. \quad (\text{C3})$$

Therefore, the CG method can be summarized as follows:

$$\mathbf{r}_{(0)} = \mathbf{b} - \mathbf{A}\mathbf{x}_{(0)} \quad (\text{C4})$$

$$\mathbf{d}_{(0)} = \mathbf{b} - \mathbf{A}\mathbf{x}_{(0)} \quad (\text{C5})$$

$$\alpha_{(i)} = \frac{\mathbf{r}_{(i)}^T \mathbf{r}_{(i)}}{\mathbf{d}_{(i)}^T \mathbf{A} \mathbf{d}_{(i)}} \quad (\text{C6})$$

$$\mathbf{x}_{(i+1)} = \mathbf{x}_{(i)} + \alpha_{(i)} \mathbf{d}_{(i)} \quad (\text{C7})$$

$$\mathbf{r}_{(i+1)} = \mathbf{r}_{(i)} - \alpha_{(i)} \mathbf{A} \mathbf{d}_{(i)} \quad (\text{C8})$$

$$\beta_{(i+1)} = \frac{\mathbf{r}_{(i+1)}^T \mathbf{r}_{(i+1)}}{\mathbf{r}_{(i)}^T \mathbf{r}_{(i)}} \quad (\text{C9})$$

$$\mathbf{d}_{(i+1)} = \mathbf{r}_{(i+1)} - \beta_{(i+1)} \mathbf{A} \mathbf{d}_{(i)} \quad (\text{C10})$$

The interesting feature of the CG method is that each subsequent correction to the solution vector is orthogonal

to all previous ones, while at the same time it points into the direction where the error in the solution decreases most quickly. This normally produces a comparatively rapid convergence of the scheme.

### REFERENCES

- Abel T., Norman M. L., Madau P., 1999, *ApJ*, 523, 66  
 Abel T., Wandelt B. D., 2002, *MNRAS*, 330, L53  
 Altay G., Croft R. A. C., Pelupessy I., 2008, *MNRAS*, 386, 1931  
 Alvarez M. A., Bromm V., Shapiro P. R., 2006, *ApJ*, 639, 621  
 Aubert D., Teyssier R., 2008, *MNRAS*, 387, 295  
 Bolton J. S., Viel M., Kim T.-S., Haehnelt M. G., Carswell R. F., 2008, *MNRAS*, 386, 1131  
 Cen R., 1992, *ApJS*, 78, 341  
 Cen R., 2002, *ApJS*, 141, 211  
 Ciardi B., Ferrara A., Marri S., Raimondo G., 2001, *MNRAS*, 324, 381  
 Ciardi B., Stoehr F., White S. D. M., 2003, *MNRAS*, 343, 1101  
 Croft R. A. C., Altay G., 2008, *MNRAS*, 388, 1501  
 Fan X., 2007, in Metcalfe N., Shanks T., eds, *Cosmic Frontiers Vol. 379 of Astronomical Society of the Pacific Conference Series, The Highest Redshift Quasars: Early Black Hole Growth and the End of Reionization Epoch.* p. 35  
 Fan X., et al., 2006, *AJ*, 131, 1203  
 Finlator K., Ozel F., Dave R., 2008, (*astro-ph/0808.3578*)  
 Gnedin N. Y., Abel T., 2001, *New Astronomy*, 6, 437  
 Gnedin N. Y., Ostriker J. P., 1997, *ApJ*, 486, 581  
 Iliev I. T., Ciardi B., Alvarez M. A., Maselli A., Ferrara A., Gnedin N. Y., Mellema G., Nakamoto T., Norman M. L., Razoumov A. O., Rijkhorst E.-J., Ritzerveld J., Shapiro P. R., Susa H., Umemura M., Whalen D. J., 2006, *MNRAS*, 371, 1057  
 Iliev I. T., Mellema G., Pen U.-L., Merz H., Shapiro P. R., Alvarez M. A., 2006, *MNRAS*, 369, 1625  
 Iliev I. T., Shapiro P. R., Raga A. C., 2005, *MNRAS*, 361, 405  
 Jubelgas M., Springel V., Dolag K., 2004, *MNRAS*, 351, 423  
 Kohler K., Gnedin N. Y., Hamilton A. J. S., 2007, *ApJ*, 657, 15  
 Kunasz P., Auer L. H., 1988, *Journal of Quantitative Spectroscopy and Radiative Transfer*, 39, 67  
 Li Y., Hopkins P. F., Hernquist L., Finkbeiner D. P., Cox T. J., Springel V., Jiang L., Fan X., Yoshida N., 2008, *ApJ*, 678, 41  
 Maselli A., Ferrara A., Ciardi B., 2003, *MNRAS*, 345, 379  
 Mellema G., Iliev I. T., Alvarez M. A., Shapiro P. R., 2006, *New Astronomy*, 11, 374  
 Mellema G., Raga A. C., Canto J., Lundqvist P., Balick B., Steffen W., Noriega-Crespo A., 1998, *A&A*, 331, 335  
 Mihalas D., Weibel Mihalas B., 1984, *Foundations of radiation hydrodynamics*. New York: Oxford University Press, 1984  
 Monaghan J. J., 1992, *ARA&A*, 30, 543  
 Nakamoto T., Umemura M., Susa H., 2001, *MNRAS*, 321, 593

- Osterbrock D. E., Ferland G. J., 2006, *Astrophysics of gaseous nebulae and active galactic nuclei*. *Astrophysics of gaseous nebulae and active galactic nuclei*, 2nd. ed. by D.E. Osterbrock and G.J. Ferland. Sausalito, CA: University Science Books, 2006
- Pawlik A. H., Schaye J., 2008, *MNRAS*, 389, 651
- Razoumov A. O., Cardall C. Y., 2005, *MNRAS*, 362, 1413
- Rijkhorst E.-J., Plewa T., Dubey A., Mellema G., 2006, *A&A*, 452, 907
- Ritzerveld J., Icke V., Rijkhorst E.-J., 2003, (*astro-ph/0312301*)
- Shapiro P. R., Iliev I. T., Raga A. C., 2004, *MNRAS*, 348, 753
- Shin M.-S., Trac H., Cen R., 2008, *ApJ*, 681, 756
- Sokasian A., Abel T., Hernquist L. E., 2001, *New Astronomy*, 6, 359
- Sokasian A., Yoshida N., Abel T., Hernquist L., Springel V., 2004, *MNRAS*, 350, 47
- Springel V., 2005, *MNRAS*, 364, 1105
- Springel V., Hernquist L., 2002, *MNRAS*, 333, 649
- Springel V., Yoshida N., White S. D. M., 2001, *New Astronomy*, 6, 79
- Susa H., 2006, *PASJ*, 58, 445
- Trac H., Cen R., 2007, *ApJ*, 671, 1
- Whalen D., Norman M. L., 2006, *ApJS*, 162, 281
- White R. L., Becker R. H., Fan X., Strauss M. A., 2003, *AJ*, 126, 1
- Whitehouse S. C., Bate M. R., 2004, *MNRAS*, 353, 1078
- Whitehouse S. C., Bate M. R., Monaghan J. J., 2005, *MNRAS*, 364, 1367
- Wise J. H., Abel T., 2008, *ApJ*, 684, 1
- Yoshida N., Oh S. P., Kitayama T., Hernquist L., 2007, *ApJ*, 663, 687
- Zahn O., Lidz A., McQuinn M., Dutta S., Hernquist L., Zaldarriaga M., Furlanetto S. R., 2007, *ApJ*, 654, 12

This paper has been typeset from a  $\text{\LaTeX}$  file prepared by the author.